Adhikari, S., Caron, L., Steinberger, B., Reager, J. T., Kjeldsen, K. K., Marzeion, B., Larour, E., Ivins, E. R. (2018): What drives 20th century polar motion? - *Earth and Planetary Science Letters*, *502*, pp. 126—132.

DOI: http://doi.org/10.1016/j.epsl.2018.08.059

What drives 20th century polar motion?

Surendra Adhikari[a,*], Lambert Caron[a], Bernhard Steinberger[b,c], John T. Reager[a], Kristian K. Kjeldsen[d,e], Ben Marzeion[f], Eric Larour[a], Erik R. Ivins[a]

[a]*Jet Propulsion Laboratory, California Institute of Technology, Pasadena, California, USA*
[b]*GFZ German Research Centre for Geosciences, Potsdam, Germany.*
[c]*Centre for Earth Evolution and Dynamics, University of Oslo, Oslo, Norway.*
[d]*Department of Geodesy, Technical University of Denmark, Kongens Lyngby, Denmark.*
[e]*Geological Survey of Denmark and Greenland, Copenhagen, Denmark.*
[f]*Institute of Geography, University of Bremen, Bremen, Germany.*

Abstract

Astrometric and geodetic measurements show that the mean position of Earth's spin axis drifted through the solid crust toward Labrador, Canada at an average speed of 10.5 ± 0.9 cm/year during the 20th century. Understanding the origins of this secular polar motion (SPM) has significance for modeling the global climate, as it provides a link to ice mass balance and sea-level rise. A perplexing issue, however, is that while glacial isostatic adjustment (GIA) models satisfactorily explain the direction of SPM, the associated prediction of the amplitude is insufficient. Our Bayesian GIA analysis, with constraints from relative sea-level and vertical land motion data, reveals that this process only accounts for $33 \pm 18\%$ of the observed SPM amplitude. This shortfall motivates a more broadly scoped reassessment of SPM drivers. To address this, we assemble a complete reconstruction of Earth's surface mass transport derived from recent advancements in modeling the global 20th century cryospheric, hydrologic, oceanic, and seismogenic mass exchange. The summed signals, nonetheless, cannot fully reconcile the observed SPM, even when considering the error statistics of each driver. We investigate an additional excitation source: changes in Earth's inertia tensor caused by mantle convection. Sophisticated models

*Corresponding author
Email address: surendra.adhikari@jpl.nasa.gov (Surendra Adhikari)
URL: https://science.jpl.nasa.gov/people/Adhikari/ (Surendra Adhikari)

have recently been advanced in tectonic plate reconstructions, in conjunction with geoid and seismic tomographic models. Here we use these models to compute new estimates of SPM. While the convection-driven SPM has considerable uncertainty, the average direction of 283 recent models aligns with the residual SPM (within $2.7° \pm 14.8°$), significantly reducing the gap between observation and prediction. We assert that one key mechanism for driving 20th century SPM is long-term mass movement due to mantle convection.

Keywords: Earth rotation, polar motion, glacial isostatic adjustment, surface mass transport, mantle convection

---

1. Introduction

The study of the movement of Earth's spin axis through the Earth's crust in the astrometric and space geodetic observing era (1899-present) may be divided into at least four elements that differ by their respective timescales: hours to weeks generally involve tides, winds and atmospheric/oceanic forcings; annual and 433-day Chandler periods involve global solar related forcing and a free wobble, respectively; interannual, interdecadal and 30-year Markowitz periods involve global hydrological and cryospheric forcings, possibly modified by a subtle core-mantle coupling. The subject of this paper involves the remaining timescale of observation: a secular movement of the spin axis since 1899. Combining all available estimates [1] suggests that the spin axis drifted along $74.2° \pm 4.7°$ west longitude at a speed of 10.5 ± 0.9 cm/year during the 20th century (Figure 1a). The basic theoretical relationship of Earth's surface and interior mass transport and changes to the inertia tensor, and hence polar motion, is well known [2, 3, 4, 5, 6, 7]. The question, however, is the following: which aspects of mass transport are dominant drivers of the 20th century SPM?

Here we analyze two of the Earth's interior viscous mass transport processes that have much longer timescales than the polar motion observations themselves: GIA and mantle convection that operate on timescales of thousands to tens of millions of years. In addition, we comprehensively account for contemporary environmental forcings that involve global surface mass transport (e.g., glaciers and ice sheets imbalances, sea-level change) and the net effects of seismic deformation, in order to deliver a new, multidisciplinary, and unified explanation to the 20th century polar motion.

2. Glacial isostatic adjustment

It has been argued throughout the last four decades that slow viscous mantle flow in response to many cycles of Late Pleistocene glaciation drives the observed SPM [2, 3, 6]. For a reasonable choice of deglaciation history, solid Earth structure, and material parameters (especially lower mantle viscosity), it is indeed possible to construct a GIA model that matches both the direction and amplitude of observed SPM almost entirely (Figure 1a). This simple explanation, however, is highly problematic because it ignores the changes in Earth's inertia tensor accompanying an unequivocal rise in global mean sea-level (GMSL) during the 20th century [8, 9]. One recent breakthrough in our understanding of GIA processes, for example, is the recognition of an important restoring torque due to the background long-term triaxiality of the Earth's inertia tensor [7]. Such necessary improvements in the GIA model generally dampen the predicted SPM amplitudes (Figure 1a). Consequently, it has become rather widely accepted that non-GIA processes should be integral to explaining the observed SPM [10, 11, 12]. Quantifying the relative importance of such contributions, however, has been hampered by the relatively poorly treated statistics of the GIA predictions of SPM.

Here we employ a GIA model [13] that operates on a robust Bayesian statistical framework (Supplementary Methods Section 1). Our model has a radially symmetric solid Earth structure, with one lithosphere and two mantle layers, that may be sufficient to evaluate statistics of low-degree gravity coefficient change and resulting polar motion. We assemble a global distribution of paleo relative sea-level (RSL) data from 11,451 sites and Global Positioning System (GPS) data from 459 stations. We have carefully selected these data sets and corrected, when applicable, for contemporary ice loss to ensure that these are minimally contaminated by non-GIA signals. We build a cost function, to be minimized, by ingesting all of these global data sets into our Bayesian framework, with a proper accounting of data uncertainty and redundancy, in order to explore parameter space related to solid Earth structure and deglaciation history simultaneously. One approach often taken is to use the observed polar motion as a necessary constraint on lower mantle viscosity structure [14]. Here we do not provide such rotational constraints because our goal is to cleanly quantify GIA-driven SPM, given that other drivers are present. Our Bayesian analysis therefore unburdens the GIA model from seeking full reconciliation of observed SPM. What emerges is the probability distribution function – based on a set of 128,000 model realizations – for the present rate of GIA-driven SPM (Figure 1b).

It is important to appreciate the sensitivity of the predicted SPM with respect to the GIA model parameters. Here we explore a total of eight parameters (Figure 2), three of which are related to solid Earth structure and five to the relative ice volumes involved in deglaciation since the Last Glacial Maximum. The glaciation parameters basically scale the ice volume of the reference ice models [15, 16] in five different regions independently. Figure 2 suggests the following two key points: (1) as noted in past studies [2, 6, 11, 12], SPM predictions are most sensitive to lower mantle viscosity; and (2) as depicted by the clustering of "likely" models, all of the model parameters are fairly well resolved by the constraining data sets. Our preferred models have upper and lower mantle viscosities in the respective ranges of $(3.6 - 10) \times 10^{20}$ Pa s and $(7 - 73) \times 10^{21}$ Pa s. These are in agreement with the average profiles of many GIA models [10, 15, 16], including those that account for rotational constraints [12], and with a number of mantle convection models, some of which are considered later in this study [17]. Our estimates are also consistent with viscosities inferred, for example, from Satellite Laser Ranging measurements of low-degree gravity field [18], mineral physics [19], and sinking rate of subducted lithosphere [20].

We estimate that GIA presently causes the Earth's spin axis to drift along

$79.4° \pm 2.9°$ west longitude at a speed of 3.5 ± 1.9 cm/year, accounting for only $33 \pm 18\%$ of the observed SPM amplitude. Predicted direction, as in many GIA models [3, 11], aligns well with the observation with a difference of only $5.2° \pm 5.5°$. Our estimate of SPM amplitude is within the plausible range of estimates recently computed using the improved theory of ice age Earth's rotation [7, 10, 11, 12]. For example, a theoretical model accounting for a restoring torque associated with the triaxiality of the Earth's inertia tensor [10] predicts that GIA cannot explain more than 70% of the observed SPM. Whereas another model, constrained by secular rate of degree-2 zonal gravity coefficient, having a low viscosity D" layer above the core-mantle boundary [12] predicts an even smaller contribution from GIA ($\sim 45\%$). It is important to recognize that our estimates are independently derived using a Bayesian approach to assimilate a global distribution of $\sim 12,000$ RSL/GPS data, and hence represent the statistically most robust estimates available to date.

3. Environmental processes

Considering the recent discovery that the transfer of mass between the continents and oceans may dramatically shift the general drift direction of Earth's spin axis [21, 22], we assess the effect of environmental processes on the 20th century SPM. Climate reconstructions that account for land-ocean mass transport are essential to deciphering the anthropogenic signals in the data record. Consequently, 20th century atmospheric, land hydrology, ocean heat exchange and cryospheric mass balance reconstructions have made significant advancement in the past decade. Each potential contributor to the 20th century GMSL rise is now robustly estimable [23, 24, 25, 26, 27], including those which are by direct human intervention [23, 24]. We collect all sources of continental mass changes (Table 1) and solve for the associated ocean mass redistribution, constrained by the mass conservation principle, on an elastically compressible, self-gravitating, rotating Earth [28] to develop a complete global model of Earth's surface mass transport and robustly quantify the associated SPM (Supplementary Methods

Section 2).

The response is considered for global glaciers that include 18 of the 19 regions of the Randolph Glacier Inventory (RGI). This part of the cryosphere has been modeled using the 20th century climate data [26] and been shown to be consistent with glaciological observations (e.g., surface mass balance, glacier volume change). The 20th century evolution of the Greenland Ice Sheet, with high-resolution maps of ice thinning, has been constrained by combining aerial imagery and measurements form airborne and satellite altimetry [25]. While the evolution of Antarctic Ice Sheet and its peripheral glaciers – the 19th RGI region – are more uncertain, several lines of evidence suggest that much of the Antarctic Peninsula has been losing mass since the Little Ice Age maximum [29, 30], the West Antarctica (and the Amundsen Sea Sector especially) has been thinning at least since the 1930s [27], and East Antarctica has remained mostly stable, with its outlet glaciers fluctuating on interdecadal timescales [31] and its surface mass balance showing no apparent trends [32], at least during the latter half of the 20th century.

In addition to these cryospheric sources, the 20th century rise in GMSL has also been affected by sustained changes in terrestrial water storage, primarily related to ground water depletion and artificial reservoir water impoundment. Model-based, observationally-constrained global estimates of ground water depletion [24] show accelerated mass loss in the continental US and the Indian subcontinent throughout the 20th century. Total reservoir water impoundment – based on the storage capacity and seepage potential of the world's 29,000 large dams – is estimated to be significant enough to lower the 20th century GMSL rise by about 29 mm [23]. Other anthropogenic terrestrial sources (e.g., deforestation, wetland and endorheic basin storage loss) are nominal, and changes in natural storage (e.g., soil moisture, permafrost, snow) are assumed to be limited to interannual to decadal variability [33]. The combined cryospheric and hydrologic contributions falls short of the more likely rate of the 20th century GMSL: 1 to 2 mm/year (Table 1). We consider the residual as a steric sea-level change that may also redistribute the ocean mass internally, inducing a non-negligible

SPM [34].

Our estimates of SPM driven by all sea-level sources mentioned above, and accompanying ocean mass redistributions, show greatly varying amplitudes and directions (Figure 3). High-mountain Asian glaciers, together with those in the Southern Andes, play a stronger role than do the combined effects of Alaskan and peripheral Greenland glaciers in controlling the net SPM associated with global glaciers and ice caps. We assume that atmospheric excitations (due to winds and surface pressure variations) are negligible on secular timescales [1]. Our estimate of the sum of all environmental processes is that they drive a net SPM along $19.2^\circ \pm 16.1^\circ$ east longitude at a speed of 4.3 ± 1.0 cm/year averaged over the 20th century (Table 1). This environmental polar motion during 2003-2015 points slightly eastwards (along 27.7° east longitude) but at a much faster rate (14.2 cm/year) [22], revealing a global geodetic imprint of accelerated mass loss from Greenland, West Antarctica, and ground water. We emphasize the importance of global mass conservation (i.e., inclusion of induced ocean mass redistribution due to self-attraction and loading), as it accounts for about 27% of the environmental SPM amplitude, with minimal effects on the predicted direction.

4. Residual motion and mantle convection

Coseismic and interseismic deformations tend to operate in opposing directions and the sum yields a small excitation (on the order of 0.8 cm/year along 117° west longitude) during the 20th century [35]. The summed GIA, environmental and seismogenic signals – when subtracted from the observed SPM – yields a residual motion that points along $101.1^\circ \pm 9.7^\circ$ west longitude at a speed of 7.4 ± 2.4 cm/year (Figure 4). Finally, to explain this large residual, we are compelled to turn to inertia changes owing to mantle convection.

Over geological timescales, global plate motions are reconstructed from geomagnetic reversals recorded at mid-ocean ridges and hotspot tracks. Combining these with paleomagnetic data from the continents, the “true” position of the spin axis can be deduced [36], as it aligns with the Earth's magnetic dipole. This "True Polar Wander" (TPW) can be modeled geodynamically, because the spin axis follows the maximum inertia axis, which can be determined from the degree-2 geoid. Although advanced geodynamical models now incorporate the delayed viscous adjustment of the rotational bulge [37, 17], we mostly disregard this effect here. This is because the adopted viscosities and the inferred rates of TPW are such that the spin axis should follow very closely the maximum inertia axis associated with mantle convection [38], as confirmed by the one case considered in our calculations where the effect of rotational bulge adjustment is investigated. The evolving density anomalies in geodynamical models, which give rise to geoid changes, can be inferred from global subduction histories and the sinking rate of slabs [39, 17], or from density and flow models [40, 38] based on seismic tomographic observations [41].

Here, we assemble "present" rates of TPW – termed mantle convection driven SPM – computed by contemporary geodynamical models without an *a priori* goal of reconciling the residual SPM (Supplementary Methods Section 3). We retrieve 94 modeled rates of TPW, each for the last 2 and 10 million years, from a suite of slab subduction driven forward models that were based on plate motions and aimed at reconstructing 3-D seismic structure and the geoid [17]. These are computed assuming a realistic viscosity structure [19], which is compatible with – though not precisely the same as – the inferred viscosity profile in our GIA Bayesian inversions [13]. We also perform a total of 95 new computations using a backward-advection approach [38] that ingests a suite of seismic tomographic models and viscosity structures toward reconstructing the past plate motions. We vary a set of key parameters (e.g., tomographic models, viscosity structure, factors that translate seismic velocities into density anomalies) and adjust either the degree-2 geoid coefficients to match the actual present-day coefficients or shift the TPW curve itself to match the present-day pole position. We retrieve the predictions of TPW rate for the last 0.01 or 1 million years and find that these solutions give broadly similar results as those of forward models: westward motion of the spin axis with a large spread in speed. Note that TPW rates are originally computed in "mantle reference frame", which are later projected onto the "mean lithospheric reference frame" in which both the observed and modeled SPM are evaluated.

Comparing the convection predictions to our SPM residual (Figure 4) suggests that the average model direction is, in fact, statistically indistinguishable from the SPM residual direction, with a difference of only $2.7° \pm 14.8°$. Some predictions fully reconcile the observed SPM, although these exceed TPW rates constrained by paleomagnetics [42]. We speculate that incorporating the residual SPM, either as a constraint or a diagnostic, in future mantle convection models might offer fruitful new insights to the geodynamic processes.

5. Concluding remarks

We put forth a new multidisciplinary framework to explain the 20th century polar motion. For the first time, a suite of environmental (e.g., cryospheric, hydrologic, oceanic) and solid Earth geophysical (e.g., GIA, mantle convection, seismological) processes are all brought together in an effort to explain SPM. These processes operate on a wide range of timescales, but each transports mass and perturbs the Earth's inertia tensor in an entirely quantifiable way. Our account of GIA statistics is comprehensive and the environmental processes are brought together using state-of-the-art models and data sets. Any individual mechanism only provides a partial source for the reconstruction of the SPM observations. This leads us to hypothesize that mantle convection is one key process to consider in greater detail. Indeed, our mantle convective simulations – not designed to comply with any requirements for treating 20th century polar motion – when combined with GIA, environmental and seismogenic SPM, tend to strongly reduce the misfit to the observations.

It is an open question as to how future modeling will progress to achieve a more robust reconciliation. Given the inherent uncertainties associated with seismic tomography, modeling slab density and advective history, and the general non-uniqueness in the interpretation of the low-degree geoid, we speculate that the path to a less uncertain reconciliation of SPM should involve simultaneous inversions of mantle convection and GIA, with the two solid Earth viscous components of internal mass transport treated in a rigorously consistent manner.

References

[1] R. Gross, Earth rotation variations – Long period, in: J. Herring (Ed.), Treaties on Geophysics: Physical Geodesy, Vol. 11, Elsevier, Amsterdam, 2007, pp. 215–261.

[2] R. Sabadini, W. Peltier, Pleistocene deglaciation and the Earth's rotation: implication for mantle viscosity, Geophys. J. R. Astr. Soc. 66 (1981) 553–578.

[3] P. Wu, W. Peltier, Pleistocene deglaciation and the Earth's rotation: a new analysis, Geophys. J. R. Astr. Soc. 76 (1984) 753–791.

[4] G. Spada, Y. Ricard, R. Sabadini, Excitation of true polar wander by subduction, Nature 360 (1992) 452–454.

[5] Y. Ricard, G. Spada, R. Sabadini, Polar wandering on a dynamic Earth, Geophys. J. Int. 113 (1993) 284–298.

[6] L. Vermeersen, A. Fournier, R. Sabadini, Changes in rotation induced by pleistocene ice masses with stratified analytical earth models, J. Geophys. Res. 102 (1997) 2156–2202.

[7] J. Mitrovica, J. Wahr, I. Matsuyama, A. Paulson, The rotational stability of an ice-age earth, Geophys. J. Int. 161 (2005) 491–506.

[8] W. Munk, Twentieth century sea level: An enigma, PNAS 99 (2002) 6550–6555.

[9] J. Mitrovica, C. Hay, E. Morrow, R. Kopp, M. Dumberry, S. Stanley, Reconciling past changes in Earth's rotation with 20th century global sea-level rise: Resolving Munk's enigma, Sci. Adv. 1 (2015) e1500679.

[10] G. Cambiotti, Y. Ricard, R. Sabadini, Ice age True Polar Wander in a compressible and non-hydrostatic Earth, Geophys. J. Int. 183 (2010) 1248–1264.

[11] J. Mitrovica, J. Wahr, Ice age Earth rotation, Annu. Rev. Earth Planet. Sci. 39 (2011) 577–616.

[12] M. Nakada, J. Okuno, K. Lambeck, A. Purcell, Viscosity structure of Earth's mantle inferred from rotational variations due to GIA process and recent melting events, Geophys. J. Int. 202 (2015) 976–992.

[13] L. Caron, E. Ivins, E. Larour, S. Adhikari, J. Nilsson, G. Blewitt, GIA model statistics for GRACE hydrology, cryosphere and ocean science, Geophys. Res. Lett. 45 (2018) 2203–2212.

[14] G. Kaufmann, K. Lambeck, Glacial isostatic adjustment and the radial viscosity profile from inverse modeling, J. Geophys. Res. 107 (2002) B11–2280.

[15] K. Lambeck, A. Purcell, J. Zhao, N. Svensson, The Scandinavian ice sheet: from MIS 4 to the end of the Last Glacial Maximum, Boreas 39 (2010) 410–435.

[16] K. Lambeck, H. Rouby, A. Purcell, Y. Sun, M. Sambridge, Sea level and global ice volumes from the Last Glacial Maximum to the Holocene, PNAS 11 (2014) 15296–15303.

[17] B. Steinberger, M.-L. Seidel, T. Torsvik, Limited true polar wander as evidence that Earth's nonhydrostatic shape is persistently triaxial, Geophys. Res. Lett. 44 (2017) 827–834.

[18] N. Tosi, R. Sabadini, A. Marotta, L. Vermeersen, Simultaneous inversion for the Earth's mantle viscosity and ice mass imbalance in Antarctica and Greenland, J. Geophys. Res. 110 (2005) B07402.

[19] B. Steinberger, A. Calderwood, Models of large-scale viscous flow in the Earth's mantle with constraints from mineral physics and surface observations, Geophys. J. Int. 167 (2006) 1461–1481.

[20] H. Cizkova, A. P. van den Berg, W. Spakman, C. Matyska, The viscosity of Earth's lower mantle inferred from sinking speed of subducted lithosphere, Phys. Earth Planet. Inter. 200-201 (2012) 56–62.

[21] J. Chen, C. Wilson, J. Ries, B. Tapley, Rapid ice melting drives Earth's pole to the east, Geophys. Res. Lett. 40 (2013) 2625–2630.

[22] S. Adhikari, E. Ivins, Climate-driven polar motion: 2003-2015, Sci. Adv. 2 (2016) e1501693.

[23] B. Chao, Y. Wu., Y. Li, Impact of artificial reservoir water impoundment on global sea level, Science 320 (2008) 212–214.

[24] Y. Wada, L. van Beek, F. Weiland, B. Chao, Y. Wu, M. Bierkens, Past and future contribution of global groundwater depletion to sea-level rise, Geophys. Res. Lett. 39 (2012) L09402.

[25] K. Kjeldsen, N. Korsgaard, A. Bjork, S. Khan, J. Box, S. Funder, N. Larsen, J. Bamber, W. Colgan, M. van den Broeke, M.-L. Siggaard-Andersen, C. Nuth, A. Schomacker, C. Andresen, E. Willerslev, K. Kjaer, Spatial and temporal distribution of mass loss from the Greenland Ice Sheet since AD 1900, Nature 528 (2015) 396–400.

[26] B. Marzeion, P. Laclercq, J. Cogley, A. Jarosch, Brief Communication: Global reconstructions of glacier mass change during the 20th century are consistent, The Cryosphere 9 (2015) 2399–2404.

[27] J. Smith, T. Andersen, M. Shortt, A. Gaffney, M. Truffer, T. Stanton, R. Bindschadler, P. Dutrieux, A. Jenkins, C.-D. Hillenbrand, W. Ehrmann, H. Corr, N. Farley, S. Crowhurst, D. Vaughan, Sub-ice-shelf sediments record history of twentieth-century retreat of Pine Island Glacier, Nature 541 (2017) 77–80.

[28] S. Adhikari, E. Ivins, E. Larour, ISSM-SESAW v1.0: Mesh-based computation of gravitationally consistent sea level and geodetic signatures caused by cryosphere and climate driven mass change, Geosci. Model Dev. 9 (2016) 1087–1109.

[29] A. Christ, M. Talaia-Murray, N. Elking, E. Domack, A. Leventer, C. Lavoie, S. Brachfeld, K.-C. Yoo, R. Gilbert, S.-M. Jeong, S. Petrushak, J. Wellner, the LARISSA Group, Late Holocene glacial advance and ice shelf growth in Barilari Bay, Graham Land, west Antarctic Peninsula, Vol. 31035, Geological Society of America Bulletin, 2014.

[30] A. Cook, A. Fox, D. Vaughan, J. Ferrigno, Retreating glacier fronts on the Antarctic Peninsula over the past half-century, Science 308 (2005) 541–544.

[31] B. Miles, C. Stokes, S. Jamieson, Pan-ice-sheet glacier terminus change in East Antarctica reveals sensitivity of Wilkes Land to sea-ice changes, Sci. Adv. 2 (2016) e1501350.

[32] A. Monaghan, D. H. Bromwich, R. L. Fogt, S.-H. Wang, P. A. Mayewski, D. A. Dixon, A. Ekaykin, M. Frezzotti, I. Goodwin, E. Isaksson, S. D. Kaspari, V. I. Morgan, H. Oerter, T. D. Van Ommen, C. J. Van der Veen, J. Wen, Insignificant change in Antarctic snowfall since the International Geophysical Year, Science 313 (2006) 827–831.

[33] J. Reager, A. Gardener, J. Famiglietti, D. Wiese, A. Eicker, M. Lo, A decade of sea level rise slowed by climate-driven hydrology, Science 351 (2016) 699–703.

[34] F. Landerer, J. Jungclaus, J. Marotzke, Long-term polar motion excited by ocean thermal expansion, Geophys. Res. Lett. 36 (2009) L17603.

[35] G. Cambiotti, X. Wang, R. Sabadini, D. Yuen, Residual polar motion caused by coseismic and interseismic deformations from 1900 to present, Geophys. J. Int. 205 (2016) 1165–1179.

[36] J. Besse, V. Courtillot, Apparent and true polar wander and the geometry of the geomagnetic field over the last 200 Myr, J. Geophys. Res. 107 (2002) N11–2300.

[37] G. Cambiotti, Y. Ricard, R. Sabadini, New insights into mantle convection true polar wander and rotational bulge readjustment, Earth Planet Sci. Lett. 310 (2011) 538–543.

[38] B. Steinberger, R. O'Connell, Changes of the Earth's rotation axis owing to advection of mantle density heterogeneities, Nature 387 (1997) 169–173.

[39] M. Domeier, P. Doubrovine, T. Torsvik, W. Spakman, A. Bull, Global correlation of lower mantle structure and past subduction, Geophys. Res. Lett. 43 (2016) 4945–4953.

[40] Y. Ricard, M. R. amd C. Lithgow-Bertelloni, Y. Le Stunff, A geodynamic model of mantle density heterogeneity, J. Geophys. Res. 98(B12) (1993) 21895–21909.

[41] S. French, B. Romanowicz, Whole-mantle radially anisotropic shear velocity structure from spectral-element waveform tomography, Geophys. Res. Lett. 199 (2014) 1303–1327.

[42] P. Doubrovine, B. Steinberger, T. Torsvik, Absolute plate motions in a reference frame defined by moving hot spots in the Pacific, Atlantic, and Indian oceans, J. Geophys. Res. 117 (2012) B09101.

[43] W. Peltier, Global glacial isostasy and the surface of the ice-age Earth: The ICE-5G (VM2) model and GRACE, Annu. Rev. Earth Planet. Sci. 32 (2004) 111–149.

Acknowledgements

This research was carried out at the Jet Propulsion Laboratory (JPL), California Institute of Technology, under a contract with National Aeronautics and

Space Administration (NASA), and was primarily funded through the JPL Research, Technology & Development Program (grant #01-STCR-R.17.235.118). Conversations with Felix W. Landerer are acknowledged.

Author contributions

S.A. and E.R.I. conceived the research and wrote the first draft of the manuscript. L.C. and B.S. conducted GIA and mantle convection simulations, respectively, and contributed to the interpretation of the results, as well as to the writing of the manuscript. S.A. led the rest of the calculations, with help of all other authors. All authors reviewed and approved the final draft of the manuscript.

Table 1: Sources of the 20th century GMSL rise and excitation of SPM. Components of the SPM vector are projected along the central Greenwich meridian, $\dot{m}_1$, and the 90° east longitude, $\dot{m}_2$. See Supplementary Methods Section 2 for a description on how we assemble the GMSL sources and compute SPM.

Source	GMSL rate [mm yr^{-1}]	SPM rate $\dot{m}_1$ [cm yr^{-1}]	SPM rate $\dot{m}_2$ [cm yr^{-1}]	References
Global glaciers	0.60 ± 0.04	1.46 ± 0.33	2.19 ± 0.35	[26]
Greenland Ice Sheet	0.21 ± 0.04	2.47 ± 0.92	-2.03 ± 0.68	[25]
Antarctic Ice Sheet	0.05 ± 0.04	-0.16 ± 0.29	0.69 ± 0.72	[30, 32, 29, 31, 27]
Groundwater	0.17 ± 0.04	0.77 ± 0.32	1.50 ± 0.62	[24]
Dams/reservoirs	-0.29	-0.14	-0.78	[23]
Steric	$[0.26, 1.26]$	-0.37 ± 0.28	-0.15 ± 0.12	[34]
Total	$[1.0, 2.0]$	4.03 ± 1.10	1.42 ± 1.23	

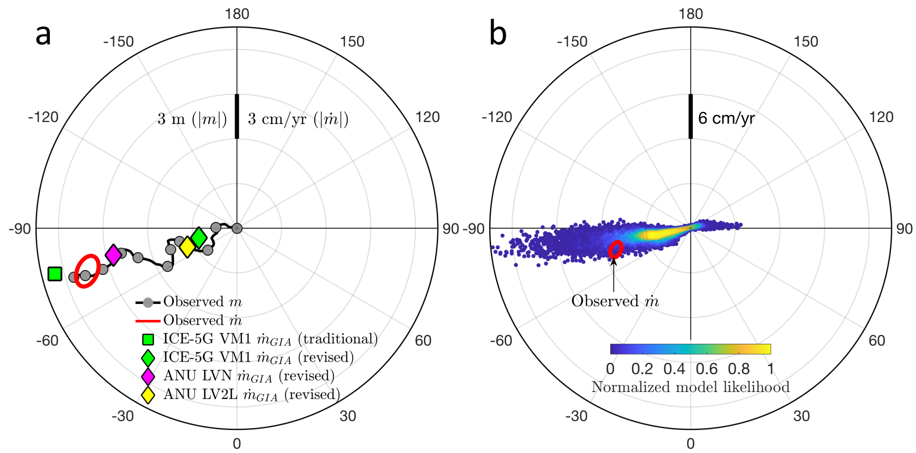

Figure 1: GIA and the 20th century SPM. **(a)** Observed and modeled rates of SPM, $\dot{m}$. All model predictions, $\dot{m}_{GIA}$, are solely due to GIA processes. The predictions differ in assumed deglaciation history (ICE-5G [43] or ANU [15, 16]) and in mantle viscosity profile (VM1 [43], LVN or LV2L [12]). The restoring torque effect is highlighted by showing predictions (green markers) computed by using the "traditional" [3] or the "revised" ice age rotational stability theory [7]. Even after accounting for the improved rotational stability, some models nonetheless predict significant $\dot{m}_{GIA}$ (magenta diamond; see also [9]). Inclusion of a low viscosity D" layer, however, dampens the amplitude (yellow diamond). This non-uniqueness in $\dot{m}_{GIA}$ solutions motivates the statistically robust new Bayesian assessment (see panel b). Observed mean pole positions, $m(t)$, relative to 1900 is shown (data courtesy of International Earth Rotation and Reference Systems Service: https://www.iers.org/) to note that the spin axis does not drift in a precisely linear path. A low pass filter having a 6-year window allows interannual signals to be seen. Gray circles represent the mean annual positions at 10-year time intervals. The same scale bar with differing metric is used for m and $\dot{m}$. **(b)** Our predicted $\dot{m}_{GIA}$ for 128,000 models. The color scale represents the likelihood of a given model to explain the global RSL/GPS data. Our predictions generally align with the observed $\dot{m}$, with many (less-likely) models fully reconciling the observation. The Bayesian statistics suggest that GIA accounts for only $33 \pm 18\%$ of the observed SPM amplitude. Note that we have different scales on panels a and b.

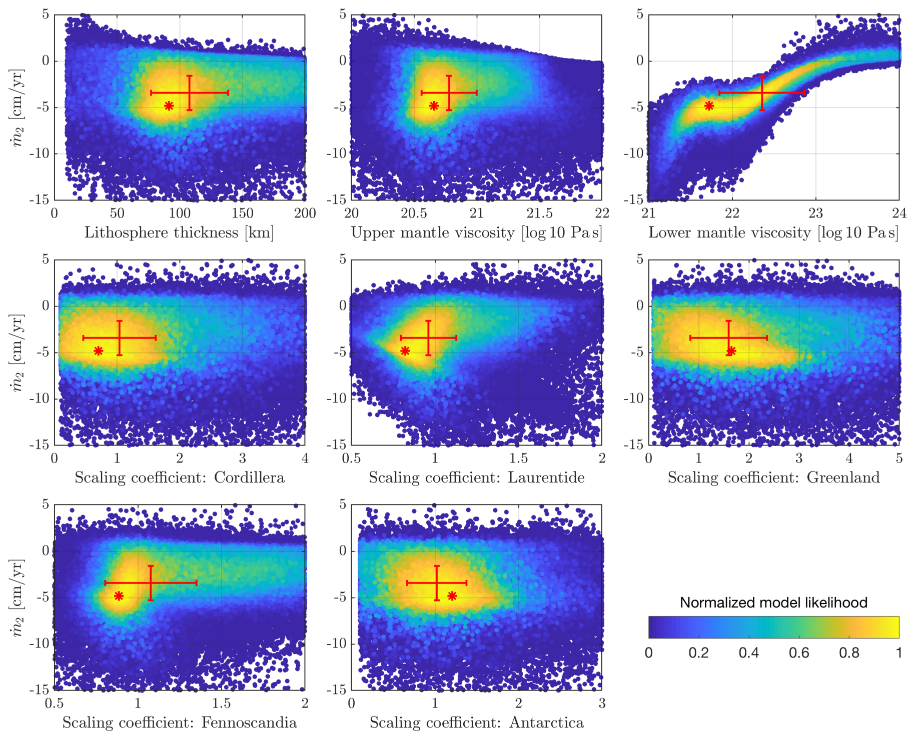

Figure 2: Sensitivity of predicted SPM with respect to GIA model parameters. To demonstrate the sensitivities in both amplitude and direction, results are shown for the SPM rate vector projected along the 90° east longitude, denoted here by $\dot{m}_2$. Likelihood probability distributions – normalized by the best-fit model probability – are projected in 2-D spaces formed by $\dot{m}_2$ and each of 8 model parameters. Both solid Earth parameters (upper panel) and relative ice volume involved in deglaciation (middle and lower panels) are considered. Stronger sensitivities are evident for lower mantle viscosity. Red stars denote the "best-fit" model solution. Expected values and 1-σ uncertainties for $\dot{m}_2$ and the model parameters are shown by vertical and horizontal error bars, respectively. Note that models with larger probability are plotted on top of those with lower probability.

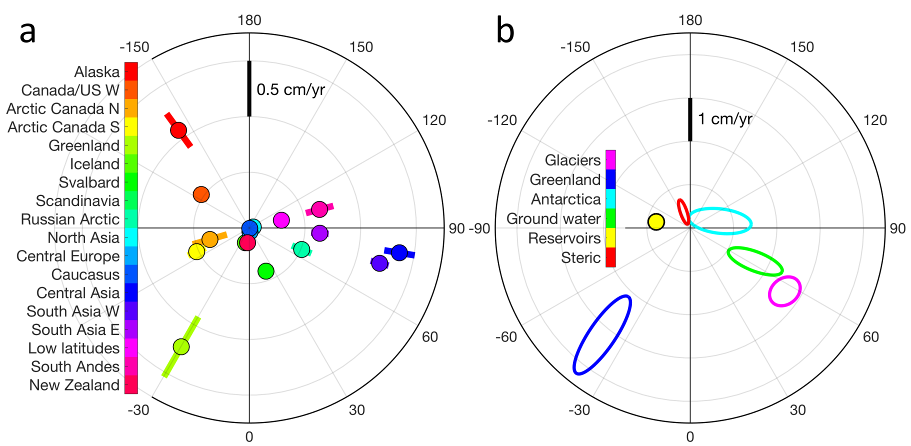

Figure 3: Environmental excitations of the 20th century SPM. **(a)** SPM driven by melting of regional glaciers and ice caps and accompanying ocean mass redistributions. For assumed uniform melting of individual RGI regions, there is no uncertainty for the predicted direction. Therefore, uncertainty estimates are provided only for the SPM amplitudes. **(b)** Combined SPM due to melting of these 18 RGI glaciated regions (pink ellipse), along with those induced by other cryospheric, hydrologic, and oceanic sources of 20th century GMSL rise (see Table 1). The ellipses represent the uncertainties. Note that we have different scales on panels a and b.

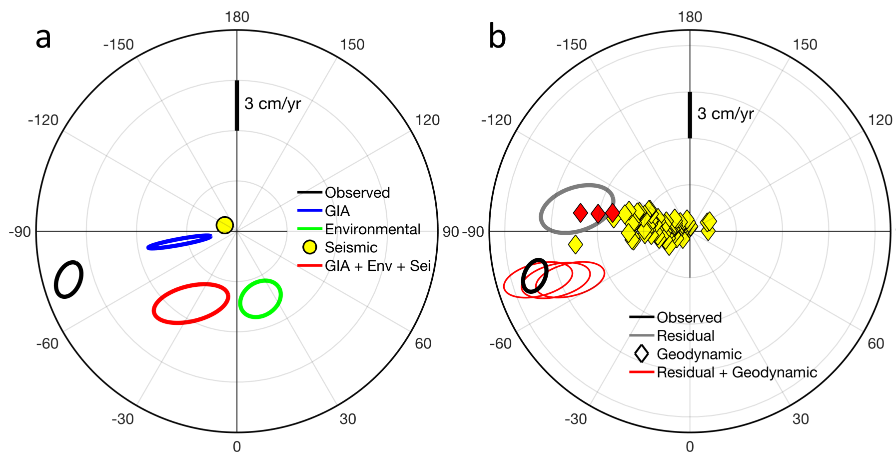

Figure 4: Budget analysis of the observed SPM. **(a)** We provide robust statistics of SPM induced by GIA and environmental processes. The summed signal (red ellipse), including seismic SPM, is far from reconciling the observation (black ellipse). **(b)** To explain large residual (gray ellipse), we assemble a total of 283 mantle convection model predictions. A full description of all of these models is given in Supplementary Methods Section 3. Here, for simplicity, we only consider 82 representative solutions (diamonds) that were retrieved for the last 0.01 million years from backward advection models. While predicted amplitudes have considerable scatter, the general direction of mantle convection driven SPM aligns with that of the residual motion. In fact, some of these predictions (e.g., red diamonds) when combined with other excitation sources tend to reconcile the observation (see black vs. red ellipses), but the associated amplitudes exceed the TPW rates constrained by paleomagnetics [42].

This document supplements our revised submission, entitled “What drives 20th century polar motion?”, and contains Methods (3 sections), 6 tables, and 9 figures.

S. Adhikari et al.

August 21, 2018

Methods

1. Glacial isostatic adjustment (GIA)

The GIA solutions used in this study are obtained following the methods of Caron *et al.* [44,13]. We use a data set of 11,451 globally distributed RSL records [15,16,45-47] and bedrock uplift trends from 459 GPS sites [48] to constrain a Bayesian inversion of GIA (Figure S1). Via a simulated annealing algorithm, we create a distribution of 128,000 GIA models by simultaneously varying solid Earth structure (i.e., lithosphere thickness, upper and lower mantle viscosities) of a radially symmetric, compressible Earth with Maxwell rheology and deglaciation history (through a set of regional scaling coefficients) (see Figure S2). Our nominal ice history model (before applying scaling coefficients) is the ANU model [25,26], except in Antarctica and Patagonia where we incorporate ice models using more contemporary constraints as described in [49-51]. All of our model constraining data sets are provided in the center-of-mass reference frame; so are the GIA computations [13].

For a given forward model, we express the cost function, J, to be minimized as follows:

$$J = \frac{1}{N}\sum_{i=1}^{N}\left[\left(y_i^d - y_i^m\right)\frac{w_i w_j}{\sigma_i}\right]^2,$$

where N is the number of data points, w_j is a weight balancing GPS and RSL data subsets, w_i is another weight accounting for redundancy of information, σ_i is the data uncertainty, y_i^m is the prediction of forward GIA model, and y_i^d is the constraining data. The GPS and RSL data subsets are considered to be *a priori* of equal importance, and the weights are such that, for equal misfit relative to the data uncertainty and without considering redundancy of information in the data set, GPS and RSL data would each account for 50% of the cost function [13]. We compute *a posteriori* probability density function (PDF), assuming a uniform prior, as follows:

$$p = \exp\left(-\frac{J}{2}\right).$$

This PDF represents how likely a given model is to explain our constraining data set as a whole, and serves as a weighing factor in our posteriori statistics of GIA parameters and signals.

For each forward GIA model, we track the position of Earth's spin axis at any time t via changes in Earth's angular velocity vector, $\mathcal{W}(t)$. In an assumed initial equilibrium state, components of angular velocity vector are given by $\mathcal{W}_i = \delta_{i3}\Omega$ (for $i = 1, 2, 3$), where δ_{i3} is the Kronecker delta and Ω is the mean rotational velocity of Earth. Following the mass redistribution on Earth's surface and within the solid Earth interior, $\mathcal{W}(t)$ is perturbed from its initial state. Let $m_i\Omega$ be the perturbation terms, where $m_i(t)$ is the normalized position of Earth's spin axis. Inserting these (and perturbation terms in Earth's inertia tensor) into the classic Euler's equation of motion for a rotating body that conserves angular momentum yields the following equation to be solved (in the Fourier frequency domain) for the relevant components of m_i [52,7]:

$$\begin{Bmatrix} m_1(\omega) \\ m_2(\omega) \end{Bmatrix} = -\gamma \frac{R^3}{GA} \begin{Bmatrix} i\omega\left(1+\alpha\dfrac{k_2^T}{k_s^T}\right)(i\omega C_{21} - \Omega S_{21}) - \alpha\Omega\left(1-\dfrac{k_2^T}{k_s^T}\right)(\Omega C_{21} + i\omega S_{21}) \\ \alpha\Omega\left(1-\dfrac{k_2^T}{k_s^T}\right)(i\omega C_{21} - \Omega S_{21}) + i\omega\left(1+\alpha\dfrac{k_2^T}{k_s^T}\right)(\Omega C_{21} + i\omega S_{21}) \end{Bmatrix}, \quad \text{(S1)}$$

where

$$\gamma = \frac{(1 + k_2^L)}{-\omega^2\left(1+\alpha\dfrac{k_2^T}{k_s^T}\right)^2 + \alpha^2\Omega^2\left(1-\dfrac{k_2^T}{k_s^T}\right)^2}$$

$\alpha = (C - A)/A$ is the Earth flattening, C is the observed polar moment of inertia, A is the observed mean equatorial moment of inertia, R is the Earth's mean radius, G is the universal gravitational constant, k_s^T is the secular tidal Love number, k_2^T is the degree-2 tidal Love number, k_2^L is the degree-2 loading Love number, C_{21} and S_{21} are the spherical harmonic coefficients of the surface load, and ω is the angular frequency.

Finally, through the inverse Fourier transform of equation (S1), we retrieve the present rate of SPM due to GIA: $\dot{m}_1$ and $\dot{m}_2$ -- components of the SPM rate vector along the central Greenwich meridian and the $90°$ east longitude, respectively. The PDF of predicted SPM (Figure 1b) is discussed in the main text. So are those that depict sensitivity of SPM with respect to GIA model parameters (Figure 2).

2. Earth's surface mass transport

Melting of land ice (glaciers, ice caps and ice sheets) and secular changes in land water storage (e.g., ground water pumping and reservoir water impoundment) do affect 20th century global sea-level [53]. To track the mean rate of mass transport between/within the continents and the oceans during the 20th century, for simplicity, we define a global mass conserving load function as follows:

$$\dot{L}(\theta,\lambda) = \rho_w\left[\dot{H}(\theta,\lambda)\mathcal{C}(\theta,\lambda) + \dot{S}(\theta,\lambda)\mathcal{O}(\theta,\lambda)\right], \qquad \text{(S2)}$$

where ρ_w is the water density, $\dot{H}(\theta,\lambda)$ is the 20th century rate of change in water equivalent height (WEH) on the continents with mask $\mathcal{C}(\theta,\lambda)$, $\dot{S}(\theta,\lambda)$ is the associated rate of change in relative sea-level with oceans mask $\mathcal{O}(\theta,\lambda)$, and (θ,λ) represents the geographic coordinates on Earth's surface. We collect $\dot{H}(\theta,\lambda)$ from several sources that are detailed below and solve for the corresponding $\dot{S}(\theta,\lambda)$ such that the resulting distribution of $\dot{L}(\theta,\lambda)$ is fully consistent with newly perturbed fields of Earth's gravitational and rotational potentials (induced by $\dot{L}(\theta,\lambda)$ itself). We consider Earth, having a fluid core, to be a self-gravitating, elastically-compressible, seismologically-constrained [54] rotating planet, whose surface gravitational and deformational response fields are parameterized via a set of Love numbers. We use methods of Adhikari *et al.* [28] that allow us to capture kilometer-scale features of $\dot{H}(\theta,\lambda)$ (e.g., mountain glaciers and dams/reservoirs) while solving for global distribution of $\dot{L}(\theta,\lambda)$, and perform all of our computations within a highly scalable, massively parallelized computational suite of Ice Sheet System Model (ISSM) [55].

Redistribution of mass on Earth's surface (equation S2) perturbs the planet's inertia tensor, $\mathcal{J}$, and hence its rotation. The relevant components of $\dot{\mathcal{J}}$ directly perturbed by $\dot{L}(\theta,\lambda)$ are given by

$$\begin{Bmatrix} \dot{\mathcal{J}}_{13} \\ \dot{\mathcal{J}}_{23} \end{Bmatrix} = -R^2 \int \dot{L}(\theta,\lambda) \sin\theta \cos\theta \begin{Bmatrix} \cos\lambda \\ \sin\lambda \end{Bmatrix} d\mathbb{S},$$

where $\mathbb{S}$ denotes the surface area of a unit sphere. Additional perturbations in $\dot{\mathcal{J}}$ arise from two major sources. First, the applied $\dot{L}(\theta,\lambda)$ induces mass redistribution within the interior of the solid Earth that may be parameterized via degree-2 load Love number as $k_2^L\, \dot{\mathcal{J}}_{i3}$ for $i = 1, 2$. Second, the associated perturbation in rotational potential further causes the solid Earth to deform and the corresponding changes in $\dot{\mathcal{J}}$ may be approximated as $\dot{m}_i(C-A)\,k_2^T/k_s^T$, where $\dot{m}_i$ (for $i = 1,2$) are the components of (rate of change in) pole position vector along the central Greenwich meridian and 90° east longitude, respectively. We assemble these perturbation terms in $\dot{\mathcal{J}}$ and define (mass) excitation functions, $\dot{\psi}_i$, as follows:

$$\dot{\psi}_i = \frac{1}{C-A}\left[\dot{\mathcal{J}}_{i3} + k_2^L\dot{\mathcal{J}}_{i3} + \frac{k_2^T}{k_s^T}(C-A)\,m_i\right].$$

For much longer timescales than 433-day Chandler wobble periods that we are interested in, excitation poles and rotational poles are virtually the same, i.e. $\psi_i \cong m_i$ [52,1], yielding

$$\begin{Bmatrix}\dot{m}_1\\ \dot{m}_2\end{Bmatrix} = \frac{k_s^T}{k_s^T - k_2^T}\frac{1+k_2^L}{C-A}\begin{Bmatrix}\dot{\mathcal{J}}_{13}\\ \dot{\mathcal{J}}_{23}\end{Bmatrix}$$

to be solved for 20th century SPM induced by Earth's surface mass transport.

As we compute and assemble SPM (and 1-σ uncertainty) associated with individual sources of Earth's surface mass transport, it is useful to note on how we formally propagate the errors. Let $X+\delta X$ and $Y+\delta Y$ be the two independent measurements. We may add these to get $Z = X + Y$ and $\delta Z = \sqrt{(\delta X)^2 + (\delta Y)^2}$, or divide to get $Z = X/Y$ and $\delta Z = |Z|\sqrt{(\delta X/X)^2 + (\delta Y/Y)^2}$.

2.1 Global glaciers and ice caps (GICs)

The response of global glaciers, contained in 18 regions of the RGI version 4.0 that does not include GrIS, AIS and peripheral Antarctic glaciers, has been modeled based on the 20th century climate observations [26] and is publicly available at http://dx.doi.org/10.5194/tc-9-2399-2015-supplement. Glacier surface mass balance models are driven by high-resolution monthly climate observations that are provided by Climate Research Unit Time-Series (CRU TS 3.22) and Climatic Research Unit Climatology (CRU CL 2.0) [56,57]. The model diagnostics (most importantly, mass balance) are shown to be consistent with glaciological observations.

We project reconstructed regional GICs mass balance [26] onto a high-resolution mesh (with element size on the order of 10 km) to generate (area-weighted) spatial distribution of 20th century ice thinning and mass loss, and solve for the associated ocean mass gain and redistribution using ISSM with 50 km resolution of global coastlines (Figure S3). Sensitivity of polar motion to regional melting of GICs is shown in Figure S4, and our estimates of 20th century SPM induced by individual RGI regions are listed in Table S1. Effects of mass conservation on SPM are also quantified, through inclusion/exclusion of induced ocean mass redistribution, as represented by $\dot{S}(\theta,\lambda)$, in a global load function $\dot{L}(\theta,\lambda)$ (see equation S2).

2.2 Greenland and Antarctic ice sheets

Observation-based estimates of 20th century evolution of GrIS are now available. Combining aerial imagery and measurements from airborne and satellite altimetry, Kjeldsen *et al.* [25] showed that GrIS has lost mass -- at a rate of -75.1 ± 29.4 Gt/year -- primarily from its fast-discharge outlets, such as Jakobshavn Isbrae and Kangerdlussuaq Glacier, during 1900-1983. A similar rate of mass loss (-73.9 ± 40.5 Gt/year) has been found for the period 1983-2003, although the bulk of the mass has been lost from the south-eastern sector of GrIS during this time period. Maps of the average rate of 20th century ice thinning and the associated ocean mass redistribution are shown in Figure S5. Note that the peripheral Greenland glaciers are included in our GICs analysis, and hence are not considered here.

The AIS and Antarctic peripheral glaciers -- not included in our GICs analysis -- evolution is more uncertain. There are several lines of evidence to suggest that parts of the Antarctic Peninsula have been losing grounded ice mass since the time of global Little Ice Age maximum [29,30,58], though glaciers of the South Shetland Islands lost mass much later [59]. Evidence points toward the West AIS in the Amundsen Sea Sector to have been thinning at least since the 1930s [27,60,61]. The East AIS has remained mostly stable at least during the latter half of the 20th century [31,32]. While East AIS outlet glaciers termini have clear evidence of multi-decadal variability [31], there are no quantifications of these into mass change. Table S2 summarizes the 20th century deglaciation history of West AIS and the Peninsula used in this study. Spatial distribution of ice loss in the Peninsula is based on the average thinning pattern of two models (model II and III) assembled by Ivins *et al.* [58] for the purpose of addressing GPS constrained GIA. The spatial pattern of the West AIS thinning is based on the measurements provided by the Gravity Recovery and Climate Experiment (GRACE), which captures essential features of 20th century evolution of the ice sheet, including the thinning around the Amundsen Sea Sector and sustained thickening upstream of Kamb Ice Stream [62]. Figure S6 shows the maps of 20th century AIS mass changes, and uncertainties therein, along with the modeled ocean mass redistribution.

Our estimates of 20th century SPM induced by GrIS and AIS (peripheral glaciers included) are summarized in Table S3. The effects of mass conservation on SPM are also quantified.

2.3 Terrestrial water storage (TWS)

Ground water depletion (GWD) and artificial reservoir water impoundment (RWI) also contributed substantially to the 20th century GMSL. Spatial distribution of 20th century mean rate of GWD and uncertainty therein [24] are shown in Figure S7, along with the modeled ocean mass variability. Large drawdown of groundwater is evident in the Middle East, Indian subcontinent, and western US. As for RWI, we collect exact location and storage information of large dams from Global Reservoir and Dam (GRanD) database (available at http://www.gwsp.org/). These dams only account for about 70% of the global reservoir storage (0.16 mm/year GMSL equivalent). For the remaining (moderate to small) dams, we rely on the compilation of Chao *et al.* [23] which, however, does not provide the specific location of dams in terms of latitude and longitude. We map the associated water storage uniformly onto the respective countries, which is sufficient for the purposes of reconstructing the relevant degree-2 pattern of loading. Following Chao *et al.* [23], we also account for TWS caused by seepage from the dams (0.07 mm/year GMSL equivalent) into adjacent rock. Figure S8 shows the spatial patterns of 20th century RWI and the associated ocean mass redistribution.

GWD and RWI (seepage included) together cause the TWS to drop (not rise) the 20th century GMSL at a rate of about 0.12 mm/year. Our estimates of associated SPM are summarized in Table S4. Effects of mass conservation on SPM are also quantified.

2.4 Internal ocean mass variability

Land (including cryospheric) contributions to the 20th century GMSL considered in our analysis (Sections 2.1-2.3) sum up to 0.74 ± 0.14 mm/year (see Table 1 in the main text). This falls short of the expected range of 1 to 2 mm/year of GMSL rise [53]. We attribute the residual to steric sea-level change that may redistribute the ocean mass internally and induce a non-negligible SPM. Based on two state-of-the-art coupled atmosphere–ocean general circulation models, Landerer *et al.* [34] demonstrated that ocean warming may lead to a specific pattern of horizontal mass redistribution -- large positive signals over the shallow shelf areas and smaller (mostly) negative signals over abyssal ocean regions -- and may induce SPM at a rate of about 0.5 cm (along $155°$ west longitude) per millimeter rise in steric GMSL. We quantify the amplitude of 20th century SPM, induced by steric sea-level rise, to be about 0.4 ± 0.3 cm/year.

3. Mantle convection

Over the timescale of æons, the Earth loses the heat of its core formation and generated by internal radioactive production. This non-equilibrium thermodynamics gives rise to buoyant convective motions of the mantle [63]. The main form of buoyancy derives from thermal differences. Imaging of the mantle by seismic waves allows estimates of the spatial configuration and magnitude of these thermal differences and associated density anomalies to be mapped in 3-D throughout the mantle [41,64-66]. In conjunction with reconstructions of plate motions [67], these models have become increasingly convincing evidence of the long-term dynamics of the mantle convective system.

Long-term polar motion is probably driven by density anomalies embedded in mantle flow [38]. As the dipole field orientation is strongly coupled to the mean rotational axis of the Earth on timescales longer than millions of years [68], this long-term polar motion can also be inferred from paleomagnetic data [36]. Mantle convection is responsible for the distortion of the core-mantle boundary (CMB) away from a hydrostatic shape by about 500 meters [69], contributing to the moments of inertia (MOI) of the Earth [70]. Further contributions are distortions of the surface (i.e., dynamic topography) and internal density anomalies, and changes in all three contribute to long-term polar wander.

The uncertainties associated with both past plate motion reconstructions and seismic imaging interpretation have been greatly reduced over the past two decades, and the details of the mantle circulation system are now being examined in numerical models. However, there are still large uncertainties in the full parameterization of such models. Using a forward, slab subduction driven, modeling approach, Steinberger *et al.* [17] explored the parameter space aimed at explaining TPW inferred from paleomagnetic data. Although this approach essentially only considers the descending limb of convection, they accounted for the effects of upwelling via simple parameterization that involves assigning an inertia tensor contribution to the Large Low Shear Velocity Provinces (LLSVPs) beneath Africa and the Pacific where the upwelling dominates and contributes a substantial degree-2 pattern in the deepest lower mantle [71]. Steinberger *et al.* [17] defined a reference model, with a particular age-depth relationship for slabs that are included to lower mantle, and varied three sets of parameters: (1) the slab age-depth relationship; (2) LLSVPs contribution to the Earth's inertia tensor; and (3) slab input models. The first set of parameters explore, for example, faster sinking in the upper mantle, slower sinking in the lower mantle, and consideration of slabs only above a certain depth (between 1400 km and CMB). The second set of parameters modify the LLSVPs contributions, for example, by varying the background inertia tensor changes between 0 and 200% of its magnitude in the reference case, by making the background inertia tensor triaxial through reduction of the intermediate MOI between 0 and 100% of the maximum MOI, or by always adjusting the background inertia tensor such that the predicted total MOI matches the present-day observations. The third set of parameters account for constant vs. variable thickness of subducted lithosphere and convergence rate [72], as well as for different plate reconstruction models [73,74]. Our retrieval of 188 solutions for "present" rate of TPW computed by these models -- 94 each for the past 2 and 10 million years -- are shown in Figure S9 and listed in Table S5.

The evolving density anomalies, and hence changes in the Earth's inertia tensor, in mantle convection models may also be inferred from seismic tomography through backward advection [38]. Here, we perform a total of 95 new computations of present rate of TPW using this modeling approach and explore the effect of some of the key parameters (Table S6; Figure S9). In all cases, it has been assured that the combination of parameters matches the present-day geoid reasonably well: variance reduction is always above 40%, in most cases above 70%. For some tomography models for which the fit is particularly good, a larger number of cases are included. In most cases, polar wander is computed with two different methods. Firstly (columns 6 and 7 in Table S6), the degree-2 geoid coefficients are adjusted such that they exactly match the present-day values, and hence the rotation pole is exactly matched. Secondly (columns 8 and 9 in Table S6), like for most cases in the forward approach [17], geoid coefficients are not modified, but the TPW curve is shifted such that it matches the north pole known at the present-day. Both cases tend to give similar azimuth, but the computed amount of motion is often quite a bit larger in the latter case. This occurs, because the computed non-hydrostatic geoid tends to be less triaxial and more "prolate" (with the long axis approximately near the centers of the LLSVPs at ~11°E, which also explains the overall preferred direction of motion, at about 90° from there), so the pole is easier to move than in the case where the geoid is set to be triaxial.

Variations of model assumptions are meant to account for uncertainties, which should hence be represented by the spread of results. Figure S9 reveals that all of the 283 models -- irrespective of the employed modeling approach and computational time steps -- yield broadly similar results for the "present" rate of TPW: westward motion of the spin axis with a large spread in amplitude. It is encouraging to note that none of these models were originally set up to study the polar motion since AD 1899, yet some of these predictions, as shown in Figure 4, reduce the gap between the observed and predicted SPM almost entirely. Since the mantle convection model parameters are varied one at a time (unlike in Bayesian GIA analysis), it leaves little justification to compute the formal statistics of the model ensembles.

References

[44] Caron, L., Metivier, L., Greff-Lefftz, M., Fleitout, L., and Rouby H., 2017, Inverting glacial isostatic adjustment signal using Bayesian framework and two linearly relaxing rheologies, *Geophys. J. Int.*, 209, 1126-1147.

[45] Dyke, A.S., Andrews, J.T., Clark, P.U., England, J.H., Miller, G.H., Shaw, J., and Veillette, J.J., 2002, The Laurentide and Innuitian ice sheets during the last glacial maximum, *Quaternary Sci. Rev.*, 21, 9-31.

[46] Milne, G.A., Long, A.J., and Bassett, S.E., 2005, Modelling Holocene relative sea-level observations from the Caribbean and South America. *Quaternary Sci. Rev.*, 24, 1183-1202.

[47] Verleyen, E., Tavernier, I., Hodgson, D.A., Whitehouse, P.L., Kudoh, S., Imura, S., Heirman, K., Bentley, M.J., Roberts, S.J., De Batist, M., Sabbe, K., and Vyverman, W., 2017, Ice sheet retreat and glacio-isostatic adjustment in Lutzow-Holm Bay, East Antarctica, *Quaternary Sci. Rev.*, 169, 85-98.

[48] Blewitt, G., Kreemer, C., Hammond, W.C., and Gazeaux, J., 2016, MIDAS robust trend estimator for accurate GPS station velocities without step detection, *J. Geophys. Res. Solid Earth*, 121, 2054-2068.

[49] Ivins, E.R., and James, T.S., 2004, Bedrock response to Llanquihue Holocene and present day glaciation in southernmost South America, *Geophys. Res. Lett.*, 31, L24613.

[50] Briggs, R.D., and Tarasov, L., 2013, How to evaluate model-derived deglaciation chronologies: a case study using Antarctica, *Quaternary Sci. Rev.*, 63, 109-127.

[51] Ivins, E.R., James, T.S., Wahr, J., Schrama, E.J.O., Landerer, F.W., and Simon, K.M., 2013, Antarctic contribution to sea-level rise observed by GRACE with improved GIA correction, *J. Geophys. Res.*, 118, 3126-3141.

[52] Munk, W.H., and MacDonald, G.J., 1960, *The Rotation of the Earth: A Geophysical Discussion*, Cambridge Univ. Press, Cambridge, 323 pages.

[53] Gregory, J.M., and 17 others, 2013, Twentieth-century global-mean sea level rise: is the whole greater than the sum of the parts? *J. Climate*, 26, 4476-4499.

[54] Dziewonski, A.M., and Anderson, D.L., 1981, Preliminary reference Earth model, *Phys. Earth Planet. Inter.*, 25, 297-356.

[55] Larour, E., Seroussi, H., Morlighem, M., and Rignot, E., 2012, Continental scale, high order, high spatial resolution, ice sheet modeling using the Ice Sheet System Model (ISSM), *J. Geophys. Res.*, 117, F01022.

[56] New, M., Lister, D., Hulme, M., and Makin, I., 2002, A high-resolution data set of surface climate over global land areas, *Clim. Res.*, 21, 1-25.

[57] Mitchell, T.D., and Jones, P.D., 2005, An improved method of constructing a database of monthly climate observations and associated high-resolution grids, *Int. J. Climatol.*, 25, 693-712.

[58] Ivins, E.R., Watkins, M.M., Yuan, D.-N., Dietrich, R., Casassa, G., and Rulke, A., 2011, On-land ice loss and glacial isostatic adjustment at the Drake Passage: 2003-2009, *J. Geophys. Res.*, 116, B02403.

[59] Simms, A.R., DeWitt, R., Ivins, E.R., Kouremenos, P., and Simkins, L.M., 2012, Determining the timing of the Little Ice Age in the Antarctic Peninsula from raised beaches, *Quaternary Sci. Rev.*, 47, 41-55.

[60] Mouginot, J., Rignot, E., Scheuchl, B., 2014, Sustained increase in ice discharge from the Amundsen Sea Embayment, West Antarctica, from 1973 to 2013, *Geophys. Res. Lett.*, 41, 1576-1584.

[61] Shepherd, A., Ivins, E.R., and the IMBIE Group, 2012, A reconciled estimate of ice-sheet mass balance, *Science*, 338, 1183-1189.

[62] Gunter, B.C., Didova, O., Riva, R.E.M., Ligtenberg, S.R.M., Lenaerts, J.T.M., King, M.A., van den Broeke, M.R., and Urban, T., 2014, Empirical estimation of present-day Antarctic glacial isostatic adjustment and ice mass change, *The Cryosphere*, 8, 743-760.

[63] Knopoff, L., 1964, The convection current hypothesis, *Rev. Geophys.*, 2, 89-122.

[64] Montelli, R., Nolet, G., Dahlen, F.A., and Masters, G., 2006, A catalogue of deep mantle plumes: New results from finite frequency tomography, *Geochem. Geophys. Geosyst.*, 7, Q11007.

[65] Fukao, Y., and Obayashi, M., 2013, Subducted slabs stagnant above, penetrating through, and trapped below the 660 km discontinuity, *J. Geophys. Res. Solid Earth*, 118, 5920-5938.

[66] French, S.W., and Romanowicz, B.A., 2015, Broad plumes rooted at the base of the Earth's mantle beneath major hotspots, *Nature*, 525, 95-99.

[67] Torsvik, T.H., Muller, R.D., van der Voo, R., Steinberger, B., and Gaina, C., 2008, Global plate motion frames: toward a unified model, *Rev. Geophys.*, 46, RG3004.

[68] Glatzmaier, G.A., and Roberts, P.H., 1995, A three-dimensional self-consistent computer simulation of a geomagnetic field reversal, *Nature*, 377, 203-209.

[69] Gwinn, C.R., Herring, T.A., and Shapiro, I.I., 1986, Geodesy by radio interferometry: Studies of the forced nutations of the earth: 2. Interpretation, *J. Geophys. Res. Solid Earth*, 91, 4755-4765.

[70] Mathews, P.M., Herring, T.A., and Buffett, B.A., 2002, Modeling of nutation and precession: New nutation series for nonrigid Earth and insights into the Earth's interior, *J. Geophys. Res.*, 107, B420068.

[71] Koelemeijer, P., Deuss, A., and Ritsema, J., 2017, Density structure of Earth's lowermost mantle from Stoneley mode splitting observations, *Nat. Commun.*, 8, 15241.

[72] Steinberger, B., and Torsvik, T.H., 2010, Toward an explanation for the present and past locations of the poles, *Geochem. Geophys. Geosys.*, 11, Q06W08.

[73] Torsvik, T.H., Steinberger, B., Gurnis, M., and Gaina, C., 2010, Plate tectonics and net lithosphere rotation over the past 150 My, *Earth Planet. Sci. Lett.*, 291, 106-112.

[74] Seton, M., Muller, R.D., Zahirovic, S., Gaina, C., Torsvik, T., Shephard, G., Talsma, A., Gurnis, M., Turner, M., Maus, S., and Chandler, M., 2012, Global continental and ocean basin reconstructions since 200 Ma, *Earth Sci. Rev.*, 113, 212-270.

[75] Steinberger, B., 2016, Topography caused by mantle density variations: observation-based estimates and models derived from tomography and lithosphere thickness, *Geophys. J. Int.*, 205, 604-621.

[76] Su, W.-J., and Dziewonski, A.M., 1994, Degree 12 model of shear velocity heterogeneity in the mantle, *J. Geophys. Res.*, 99, 6945-6980.

[77] Rudolph, M.L., Lekic, V., and Lithgow-Bertelloni, C., 2015, Viscosity jump in Earth's mid-mantle, *Science*, 350, 1349-1352.

[78] Lu, C., and Grand, S.P., 2016, The effect of subducting slabs in global shear wave tomography, *Geophys. J. Int.*, 205, 1074-1085.

[79] Megnin, C., and Romanowicz, B.A., 2000, The shear velocity structure of the mantle from the inversion of body, surface and higher modes waveforms, *Geophys. J. Int.*, 143, 709-728.

[80] Panning, M.P., and Romanowicz, B.A., 2006, A three dimensional radially anisotropic model of shear velocity in the whole mantle, *Geophys. J. Int.*, 167, 361-379

[81] Wang, S., Yu, H., Zhang, Q., and Zhao, Y., 2018, Absolute plate motions relative to deep mantle plumes, *Earth Planet. Sci. Lett.*, 490, 88-88.

Table S1 | Changes in regional ice mass, ΔM, and the predicted SPM vector for 20th century. We quantify the average contribution of induced ocean mass redistribution to SPM for individual RGI regions, $\dot{m}_i^S/\dot{m}_i$ for $i = 1, 2$. We also tabulate correlation coefficients that are required to plot error ellipses (see, e.g., Figure 3 in the main text).

RGI regions	ΔM [Gt/yr]	$\dot{m}_1$ [mm/yr]	$\dot{m}_2$ [mm/yr]	Correlation $(\dot{m}_1, \dot{m}_2)$	$\dot{m}_1^S/\dot{m}_1$ [%]	$\dot{m}_2^S/\dot{m}_2$ [%]
Alaska	-21.1 ± 3.6	-8.8 ± 1.5	-6.4 ± 1.1	1	13.2	4.7
Canada/US W	-9.3 ± 1.3	-3.0 ± 0.4	-4.3 ± 0.6	1	11.2	6.5
Arctic Canada N	-17.7 ± 7.6	1.0 ± 0.4	-3.5 ± 1.5	-1	44.8	2.6
Arctic Canada S	-13.4 ± 2.2	2.1 ± 0.4	-4.7 ± 0.8	-1	28.5	7.1
Greenland	-39.1 ± 9.9	10.7 ± 2.7	-6.1 ± 1.5	-1	22.2	0.7
Iceland	-2.6 ± 1.1	1.3 ± 0.5	-0.3 ± 0.1	-1	21.8	4.1
Svalbard	-15.6 ± 1.8	3.9 ± 0.4	1.5 ± 0.2	1	23.0	31.5
Scandinavia	-0.6 ± 0.6	0.3 ± 0.3	0.1 ± 0.1	1	18.7	24.7
Russian Arctic	-19.5 ± 3.6	1.9 ± 0.4	4.7 ± 0.9	1	30.2	19.9
North Asia	-0.7 ± 0.5	-0.1 ± 0.1	0.3 ± 0.3	-1	8.6	12.5
Central Europe	-0.5 ± 0.6	0.3 ± 0.4	0.1 ± 0.1	1	16.1	23.6
Caucasus	-0.1 ± 0.4	0.0 ± 0.2	0.0 ± 0.2	1	14.3	12.9
Central Asia	-23.8 ± 2.4	2.2 ± 0.2	13.5 ± 1.4	1	22.8	11.2
South Asia W	-21.1 ± 1.5	3.2 ± 0.2	11.7 ± 0.8	1	18.4	11.2
South Asia E	-12.2 ± 1.5	0.5 ± 0.1	6.3 ± 0.8	1	41.6	11.9
Low latitudes	-8.8 ± 0.6	-0.7 ± 0.0	2.9 ± 0.2	-1	-10.1	23.1
South Andes	-9.8 ± 1.9	-1.7 ± 0.3	6.3 ± 1.2	-1	7.3	22.0
New Zealand	-1.9 ± 0.3	1.3 ± 0.2	-0.2 ± 0.0	-1	24.1	-13.8
Total GICs	-218 ± 14	14.6 ± 3.3	21.9 ± 3.5	-0.23	36.7	27.8

Table S2 | 20th century deglaciation history for AIS used in this analysis. The West AIS estimates are collected from a number of sources (referenced in the table), the Peninsula estimates are based on two models (model II and III) of Ivins *et al.* [58], and the East AIS is assumed to have evolved minimally during the time period considered in this analysis [31,32].

West AIS	1900-1974	1974-1992	1992-2000	1900-2000
ΔM [Gt/yr]	-2 ± 17	-2 ± 17	-38 ± 32	-4.9 ± 18.7
References	[27,60]	[60]	[61]	

AIS Peninsula	1850-1930	1930-1993	1993-2000	1900-2000
ΔM [Gt/yr]	-6.0 ± 8.6	-13.0 ± 7.4	-29.6 ± 18.0	-12.1 ± 8.9

Table S3 | Changes in ice sheets and the predicted SPM for 20th century. We quantify the average contribution of induced ocean mass redistribution to SPM for individual ice sheets. We also tabulate correlation coefficients that are required to plot error ellipses.

	ΔM [Gt/yr]	$\dot{m}_1$ [mm/yr]	$\dot{m}_2$ [mm/yr]	Correlation $(\dot{m}_1, \dot{m}_2)$	$\dot{m}_1^S/\dot{m}_1$ [%]	$\dot{m}_2^S/\dot{m}_2$ [%]
GrIS	-74.9 ± 31.6	24.7 ± 9.2	-20.3 ± 6.8	-0.83	23.3	7.7
West AIS	-4.9 ± 18.7	0.6 ± 2.3	1.5 ± 5.7	1	34.9	26.8
AIS Peninsula	-12.1 ± 8.9	-2.2 ± 1.8	5.4 ± 4.4	-1	10.0	24.7
Total ice sheets	-91.9 ± 37.8	23.1 ± 9.7	-13.4 ± 9.9	-0.48	24.9	-1.3

Table S4 | Changes in TWS and the predicted SPM for 20th century. We quantify the average contribution of induced ocean mass redistribution to SPM for individual TWS components. We also tabulate correlation coefficients that are required to plot error ellipses.

	ΔM [Gt/yr]	$\dot{m}_1$ [mm/yr]	$\dot{m}_2$ [mm/yr]	Correlation $(\dot{m}_1, \dot{m}_2)$	$\dot{m}_1^S/\dot{m}_1$ [%]	$\dot{m}_2^S/\dot{m}_2$ [%]
Ground water	-61.2 ± 25.0	7.7 ± 3.2	15.0 ± 6.2	0.67	20.0	15.5
Dams/reservoirs	106.0	-1.4	-7.8	--	106.7	35.7
Total TWS	44.9 ± 25.0	6.3 ± 3.2	7.2 ± 6.2	0.67	0.7	-6.4

Table S5 | TPW computed based on subduction history. Movies and figures referred here are those from Steinberger *et al.* [17]. Rate and azimuth are listed for the last 2 million years (columns 3-4) and for 10 million years (columns 5-6). Only in the first case (Figure 2, TPW) the delayed viscous adjustment of the equatorial bulge is taken into account. Comparison with the corresponding case where it isn't (Movie S1, 0 km + 19 mm/yr*t) confirms that results for the two cases are similar. Case "2300 slow" considers slabs only to depth 2300 km, with depth-age relation 600 km + 11 mm/yr*t. Cases "const lith thick" and "const conv rate" are computed with constant lithosphere thickness and also constant convergence rate, respectively. Case MS12 is for another plate reconstruction. Some cases from the figures are not included, as they are also contained in the movies. Movie S1 and S5 cases are for different relations of depth versus time after subduction in column 2. Movie S2 and S6 are for slabs included to the maximum depth in column 2. In Movie S3, the "background" inertia tensor varies between 0 and 200% of its magnitude in the reference case. In Movie S4, the intermediate MOI of the "background" contribution varies between 0 and 100% of the maximum. For Movie S5 and S6, the background inertia tensor is chosen such that the total MOI is matched for present-day.

Figure or Movie of [17]	Case	Rate 1 [°/Ma]	Azimuth 1	Rate 2 [°/Ma]	Azimuth 2
Figure 2	TPW	0.2388	-83.81	0.1936	-83.33
Figure 3 A	2300 slow	0.0545	-86.23	0.0579	-90.40
Figure 3 E	const conv rate	0.0925	178.68	0.0838	-124.34
Figure 3 E	const lith thick	0.2330	-106.91	0.2772	-97.74
Figure 3 F	MS12	0.7018	-70.21	0.5324	-69.06
Movie S1	600 km + 11 mm/yr*t	0.0717	-75.33	0.0861	-83.09
Movie S1	525 km + 12 mm/yr*t	0.0296	158.39	0.0408	-105.77
Movie S1	450 km + 13 mm/yr*t	0.0405	167.59	0.0254	-161.52
Movie S1	375 km + 14 mm/yr*t	0.0563	-102.80	0.1339	130.46
Movie S1	300 km + 15 mm/yr*t	0.2386	122.68	0.1173	132.21
Movie S1	225 km + 16 mm/yr*t	0.1511	122.88	0.0471	-162.84
Movie S1	150 km + 17 mm/yr*t	0.0769	-89.83	0.1032	-99.98
Movie S1	75 km + 18 mm/yr*t	0.0882	-103.04	0.2202	-82.77
Movie S1	0 km + 19 mm/yr*t	0.1852	-91.66	0.2743	-79.97
Movie S2	1400 km	0.2466	-98.01	0.4029	-86.92

Movie S2	1500 km	0.2515	-96.26	0.4234	-86.30
Movie S2	1600 km	0.3503	-93.22	0.4733	-85.25
Movie S2	1700 km	0.3490	-90.90	0.4435	.83.96
Movie S2	1800 km	0.2413	-90.15	0.3805	-82.41
Movie S2	1900 km	0.2336	-89.51	0.3957	-82.51
Movie S2	2000 km	0.2885	-89.99	0.4251	-82.25
Movie S2	2100 km	0.2811	-88.69	0.4576	-80.77
Movie S2	2200 km	0.3558	-87.02	0.4765	-79.88
Movie S2	2300 km	0.3337	-84.59	0.4156	-79.56
Movie S2	2400 km	0.2612	-87.61	0.3596	-80.14
Movie S2	2500 km	0.2497	-87.973	0.3218	-80.84
Movie S2	2600 km	0.1891	-91.73	0.3003	-81.44
Movie S2	2700 km	0.2018	-91.65	0.2930	-81.06
Movie S2	2800 km	0.1894	-92.45	0.2817	-80.40
Movie S3	0 %	0.3361	-108.95	0.4223	-78.04
Movie S3	10 %	0.3041	-105.82	0.3905	-80.51
Movie S3	20 %	0.2806	-102.82	0.3692	-81.14
Movie S3	30 %	0.2622	-100.33	0.3524	-81.20
Movie S3	40 %	0.2470	-98.30	0.3380	-81.08
Movie S3	50 %	0.2340	-96.65	0.3253	-80.89
Movie S3	60 %	0.2225	-95.28	0.3136	-80.69
Movie S3	70 %	0.2119	-94.14	0.3028	-80.49
Movie S3	80 %	0.2024	-93.18	0.2927	-80.30
Movie S3	90 %	0.1935	-92.37	0.2833	-80.13
Movie S3	110 %	0.1774	-91.05	0.2658	-79.82
Movie S3	120 %	0.1701	-90.51	0.2577	-79.68
Movie S3	130 %	0.1632	-90.04	0.2501	-79.55
Movie S3	140 %	0.1567	-89.62	0.2427	-79.43
Movie S3	150 %	0.1505	-89.25	0.2357	-79.32
Movie S3	160 %	0.1447	-88.92	0.2290	-79.22
Movie S3	170 %	0.1391	-88.62	0.2226	-79.12
Movie S3	180 %	0.1338	-88.34	0.2164	-79.03
Movie S3	190 %	0.1287	-88.10	0.2105	-78.94
Movie S3	200 %	0.1239	-87.88	0.2049	-78.86

Movie S4	0 %	0.0799	-101.36	0.1439	-75.29
Movie S4	5 %	0.0835	-100.74	0.1489	-75.79
Movie S4	10 %	0.0875	-100.10	0.1543	-76.26
Movie S4	15 %	0.0919	-99.45	0.1601	-76.70
Movie S4	20 %	0.0966	-98.79	0.1663	-77.11
Movie S4	25 %	0.1017	-98.13	0.1730	-77.50
Movie S4	30 %	0.1072	-97.46	0.1802	-77.85
Movie S4	35 %	0.1133	-96.80	0.1879	-78.18
Movie S4	40 %	0.1199	-96.13	0.1963	-78.49
Movie S4	45 %	0.1270	-95.46	0.2052	-78.77
Movie S4	50 %	0.1349	-94.80	0.2149	-79.03
Movie S4	55 %	0.1435	-94.14	0.2253	-79.26
Movie S4	60 %	0.1529	-93.49	0.2365	-79.47
Movie S4	65 %	0.1632	-92.84	0.2487	-79.66
Movie S4	70 %	0.1744	-92.21	0.2619	-79.83
Movie S4	75 %	0.1868	-91.59	0.2761	-79.99
Movie S4	80 %	0.2004	-90.98	0.2916	-80.12
Movie S4	85 %	0.2153	-90.38	0.3083	-80.24
Movie S4	90 %	0.2317	-89-80	0.3265	-80.34
Movie S4	95 %	0.2497	-89.24	0.3462	-80.32
Movie S4	100 %	0.2694	-88.70	0.3675	-80.51
Movie S5	600 km + 11 mm/yr*t	0.1345	-114.09	0.1630	-117.62
Movie S5	525 km + 12 mm/yr*t	0.1055	-130.89	0.1348	-120.41
Movie S5	450 km + 13mm/yr*t	0.1225	-127.57	0.0999	-130.43
Movie S5	375 km + 14 mm/yr*t	0.1418	-115.96	0.0949	161.11
Movie S5	300 km + 15 mm/yr*t	0.1552	131.34	0.0886	163.31
Movie S5	225 km + 16 mm/yr*t	0.0974	136.30	0.1057	-138.50
Movie S5	150 km + 17 mm/yr*t	0.1284	-110.56	0.1709	-116.52
Movie S5	75 km + 18 mm/yr*t	0.1689	-116.16	0.2625	-104.66
Movie S5	0 km + 19 mm/yr*t	0.2611	-110.83	0.2966	-101.76
Movie S6	1400 km	0.1954	-96.65	0.2879	-88.48
Movie S6	1500 km	0.1960	-95.02	0.2964	-88.46
Movie S6	1600 km	0.2510	-97.23	0.3151	-89.14
Movie S6	1700 km	0.2432	-95.33	0.2900	-87.62

Movie S6	1800 km	0.1610	-92.41	0.2443	-85.90
Movie S6	1900 km	0.1555	-92.96	0.2551	-87.86
Movie S6	2000 km	0.2014	-98.31	0.2775	-90.33
Movie S6	2100 km	0.2039	-99.15	0.3003	-91.77
Movie S6	2200 km	0.2580	-101.13	0.3163	-92.76
Movie S6	2300 km	0.2567	-100.37	0.2990	-95.03
Movie S6	2400 km	0.2416	-105.81	0.2919	-97.92
Movie S6	2500 km	0.2547	-106.63	0.2859	-99.94
Movie S6	2600 km	0.2341	-110.49	0.2967	-101.97
Movie S6	2700 km	0.2657	-110.61	0.3060	-102.15
Movie S6	2800 km	0.2638	-111.30	0.3011	-101.91

Table S6 | TPW computed by backward-advecting present-day density anomalies inferred from tomography. Column 1: Tomography models (for further references see Table 1 of Steinberger [75]). Smean2 is a global, composite mantle tomography models constructed by Thorsten Becker following the approach used for Smean, but using the newer models S40RTS, GyPSUM-S and SAVANI. S5mean and S10mean are also constructed by averaging tomography models [76]. **Column 2:** Conversion to density. (1)-(3) correspond to cases 1-3 of Table 1 of Steinberger [75]. (4) accounts for possible compositional anomalies in the LLSVPs, by setting in every layer less than 300 km above the CMB density to zero if seismic velocity is less than -1%. (5)-(7) use conversion factor profile 2 of Figure 6 in Steinberger and Calderwood [19], in the top 220 km respectively (5) reduced by 50%, (6) set to zero, and (7) unmodified. (8) uses a constant conversion factor ($\partial \ln \rho / \partial \ln v_s = 0.25$) throughout the mantle. **Column 3:** Viscosity profile (VP). (S16) is optimized viscosity profiles as described, and mostly listed in Table 1 in Steinberger [75]. (1), (1b), (2) and (2b) are the respective profiles of Steinberger and Calderwood [19]. (3) is a 4-layer model with 3.0×10^{22} Pa s in the lithosphere (0-100 km), 2.8×10^{20} Pa s in the upper mantle (100-410 km), 4.7×10^{20} Pa s in the transition zone (410-660 km), and 4.3×10^{22} Pa s in the lower mantle (below 660 km), (4) is a 4-layer model with 10^{22} Pa s above 100 km, 4.0×10^{20} Pa s for 100-670 km 4.0×10^{21} Pa s for 670-1000 km and 3.0×10^{22} Pa s below 1274 km, corresponding to a mid-mantle viscosity jump proposed by Rudolph *et al.* [77]. **Column 4:** Phase boundary (PB). (y) phase boundaries are considered following Steinberger [75], (n) phase boundaries are not considered. **Column 5:** Time interval, Δt, of backward-advection. Models with $\Delta t = 1$ million years are shaded with gray. **Columns 6-9**: Rate and azimuth computed with two methods described in Section 3.

Tomography	Conv	VP	PB	Δt [Ma]	Rate 1 [°/Ma]	Azimuth 1	Rate 2 [°/Ma]	Azimuth 2
SL+Gra	1	S16	y	0.01	0.0176	14.93	0.0359	58.22
SL+Gra	2	S16	y	0.01	0.0521	−97.87	0.1688	−90.74
SL+Gra	3	2b	y	1	0.0648	−99.59		
SL+Gra	3	2b	y	0.01	0.0717	−67.70	0.1998	−72.68
SL+Gra	3	S16	y	0.01	0.0569	−113.37	0.1514	−97.88

SL+Gra	4	S16	y	0.01	0.0666	−122.95	0.1585	−104.66
Grand10	5	2b	y	0.01	0.0813	−5.30	0.1505	−35.38
Grand10	3	S16	y	0.01	0.0176	−95.01	0.1137	−92.63
Grand10	4	S16	y	0.01	0.0284	−125.58	0.1067	−101.35
TX2015 [78]	5	2b	y	1	0.1404	−82.04		
TX2015	5	2b	y	0.01	0.1267	−82.17	0.1711	−76.58
TX2015	3	S16	y	0.01	0.2241	−112.57	0.2819	−102.09
TX2015	4	S16	y	0.01	0.2178	−113.57	0.2827	−104.87
TX2015	6	2b	y	0.01	0.0846	−46.68	0.0906	−29.34
TX2015	7	2b	y	0.01	0.1885	−97.87	0.3032	−91.15
TX2015	5	2b	n	0.01	0.1177	−71.24	0.1668	−67.93
TX2015	8	2b	y	0.01	0.2721	−106.05	0.5054	−97.37
TX2015	5	2	y	0.01	0.2076	−88.61	0.2336	−82.54
TX2015	5	1	y	0.01	0.3317	−104.26	0.3511	−100.06
TX2015	5	1b	y	0.01	0.2020	−108.40	0.2404	−100.06
TX2015	5	3	y	0.01	0.1953	−97.61	0.2901	−92.65
TX2015	5	4	y	0.01	0.2693	−104.24	0.2371	−104.16
GyPSuM-S	5	2b	y	1	0.0193	22.21		
GyPSuM-S	5	2b	y	0.01	0.0160	26.83	0.1438	75.53
GyPSuM-S	3	S16	y	0.01	0.0288	117.56	0.1357	96.33
GyPSuM-S	4	S16	y	0.01	0.0352	153.78	0.1491	98.01
S20RTSb	5	2b	y	0.01	0.0197	−97.87	0.1966	−91.40
S20RTSb	3	S16	y	0.01	0.0393	72.33	0.2222	−81.45
S20RTSb	4	S16	y	0.01	0.0378	75.99	0.2092	−82.23
S40RTS	5	2b	y	1	0.0964	−65.70		
S40RTS	5	2b	y	0.01	0.0839	−65.55	0.1636	−80.24
S40RTS	3	S16	y	0.01	0.0353	−13.01	0.1066	−67.53
S40RTS	4	S16	y	0.01	0.0283	−2.08	0.0921	−67.31
Smean	8	2b	n	1	0.1949	−82.61		
Smean	8	2b	n	1	0.1746*	−78.04*		
Smean	8	2b	y	1	0.2122	−87.42		

Smean	6	2b	y	1	0.1460	−28.36		
Smean	5	2b	y	1	0.1482	−53.35		
Smean	5	2b	y	0.01	0.1392	−51.29	0.3086	−72.91
Smean	3	S16	y	0.01	0.1189	−58.91	0.3070	−76.72
Smean	4	S16	y	0.01	0.1162	−70.38	0.3286	−81.73
SE+Gra	5	2b	y	0.01	0.0587	−49.41	0.1462	−62.84
SE+Gra	3	S16	y	0.01	0.0151	−28.84	0.0602	−72.09
SE+Gra	4	S16	y	0.01	0.0122	−97.87	0.0499	−83.65
SAVANI	5	2b	y	1	0.1609	−7.59		
SAW24B16 [79]	5	2b	y	1	0.3384	−73.97		
SAW24B16	5	2b	y	0.01	0.3161	−74.25	0.6439	−79.82
SAW642an [80]	5	2b	y	0.01	0.4121	−95.06	0.2979	−93.96
SEMUCB-WM1 [41]	5	2b	y	1	0.4572	−97.94		
SEMUCB-WM1	5	2b	y	0.01	0.4232	−99.42	0.6081	−96.49
Smean2	5	2b	y	0.01	0.0565	−43.84	0.0740	−40.94
S5mean [42]	5	2b	y	0.01	0.1297	−65.93	0.2355	−76.75
S10mean [42]	5	2b	y	0.01	0.1199	−50.69	0.1664	−60.87
S12WM13 [76]	5	2b	y	1	0.3139	−45.55		

*Geoid expansion up to degree 15.

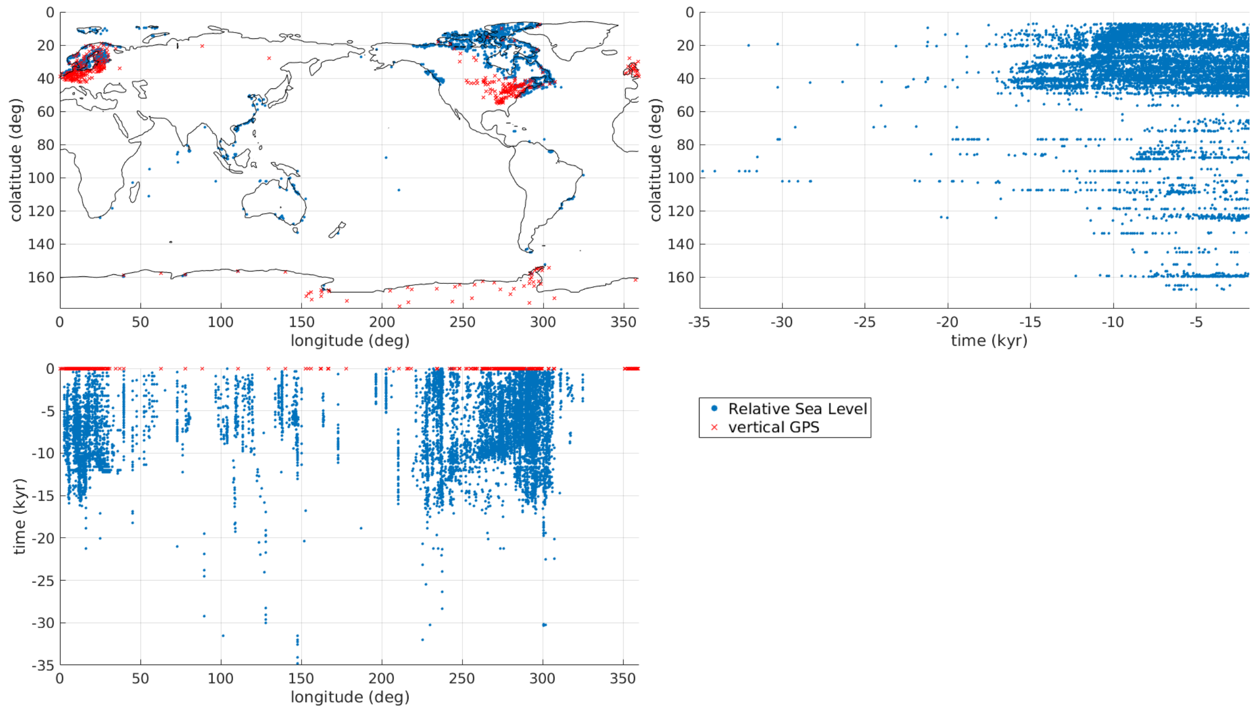

Figure S1 | Spatiotemporal distribution of RSL/GPS data used to constrain our GIA models. RSL data are obtained from [15,16,45-47] and GPS trends are from [48].

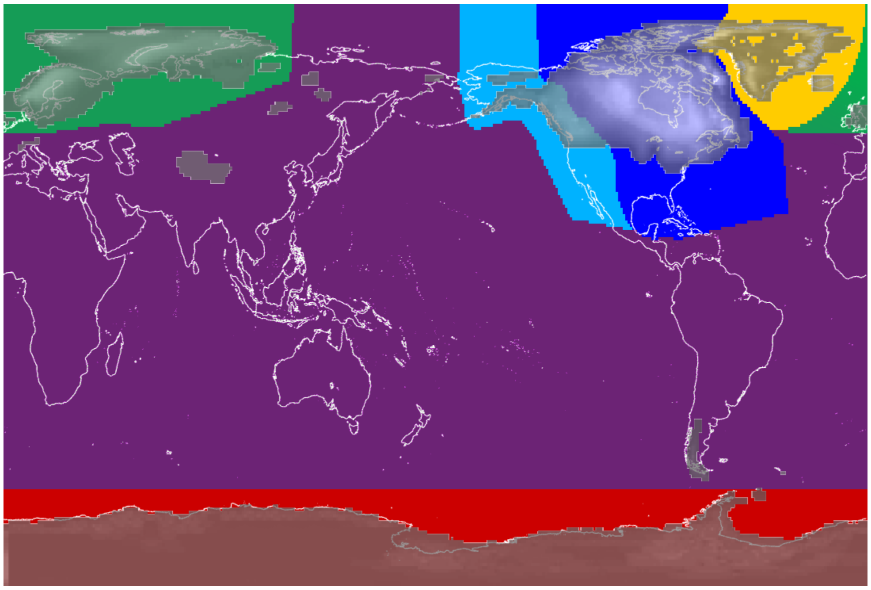

Figure S2 | Map of the different ice regions considered in the GIA inversion. Each region is indicated by a different hue. To depict the glacial extent and ice thickness maxima, we integrate the reference deglaciation model [45-47] over the last 122 kyr (shown in shades of grey). Note that the present-day ice thickness is subtracted as it does not contribute to the modern GIA; hence there are patches over GrIS for example. A Fourier transform of the time-domain allows an infinite number of glacial cycles to be included [13,44].

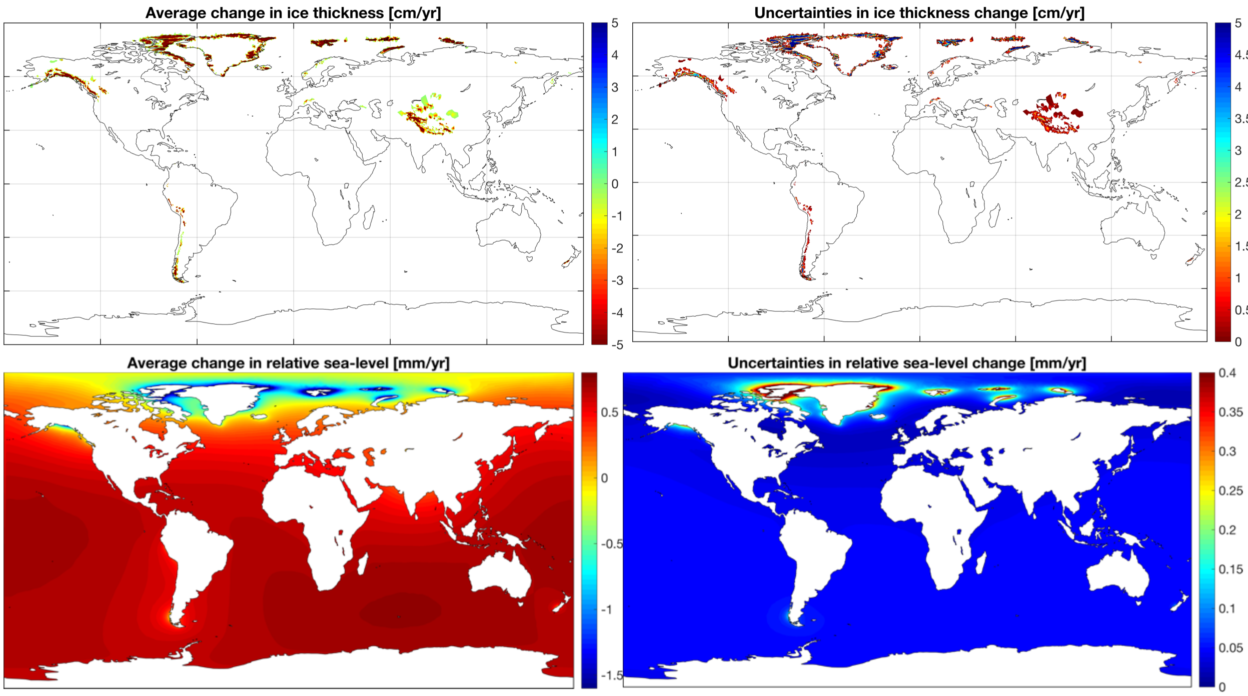

Figure S3 | GICs melting and the associated sea-level rise during the 20th century. Large ice thinning has been reconstructed for Arctic glaciers (top left). We also show the formal uncertainties (right), which reflect -- here and elsewhere in the paper -- the standard errors.

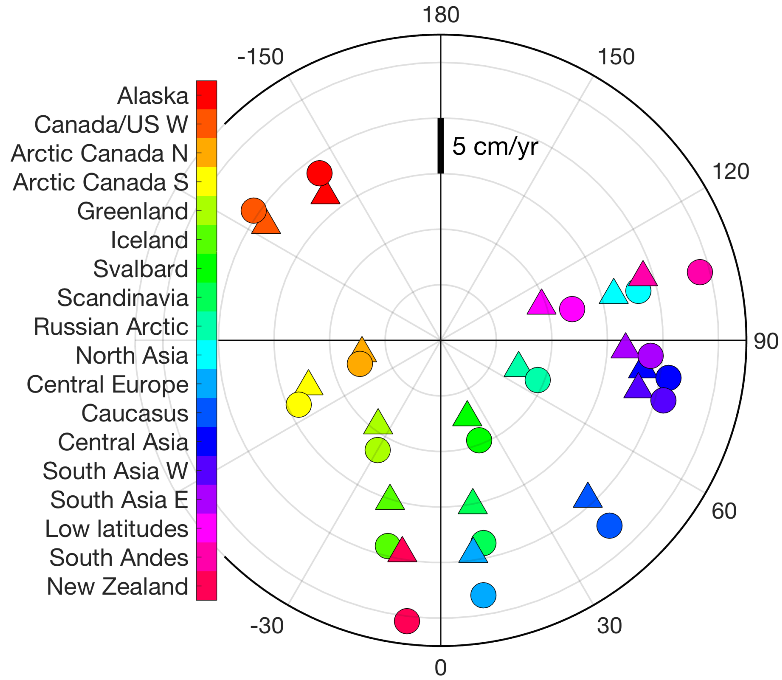

Figure S4 | Sensitivity of polar motion with respect to melting of regional GICs. Polar motions (in cm/year) are computed for 18 out of 19 RGI regions (Antarctic peripheral glaciers are excluded), assuming that uniform melting of each region raises GMSL by 1 mm/year. Polar motions excited by direct unloading of ice (triangles) and by the additional excitation induced by ocean mass redistribution (circles) (see equation S2) are both quantified.

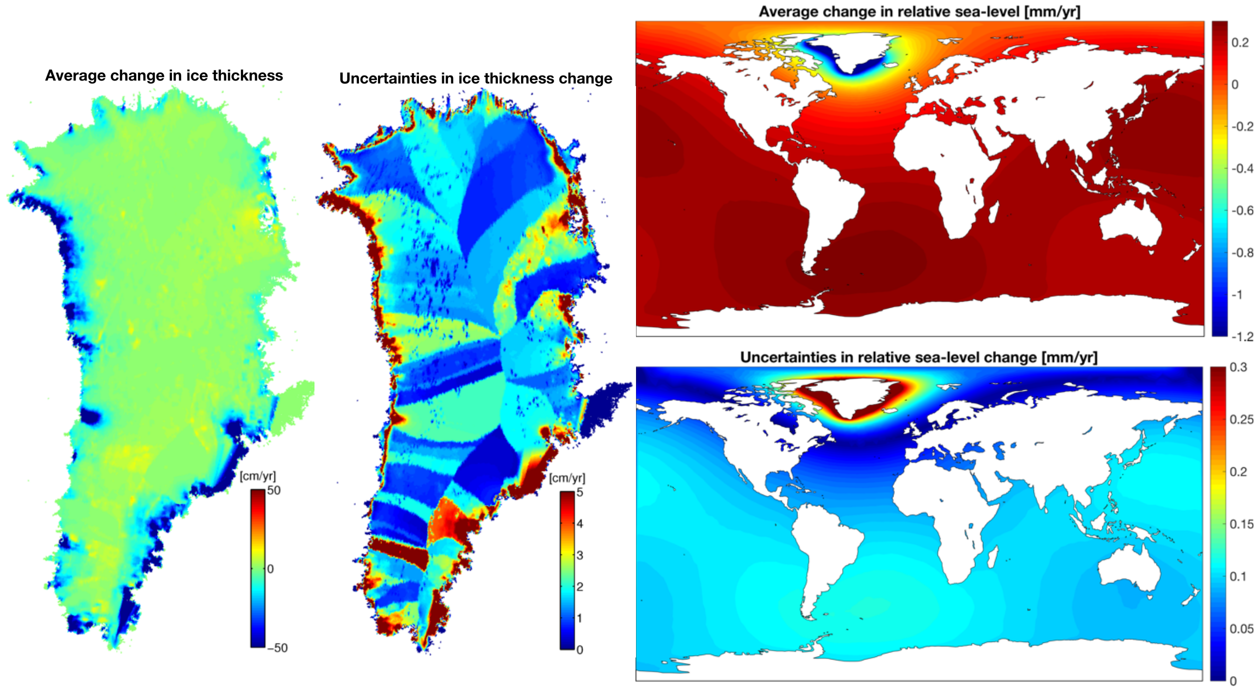

Figure S5 | GrIS thinning and the associated sea-level rise during the 20th century. The GrIS has lost its mass mostly from outlet glaciers that are located along the southeastern and northwestern sectors (left). These loss areas also have relatively large uncertainties (center).

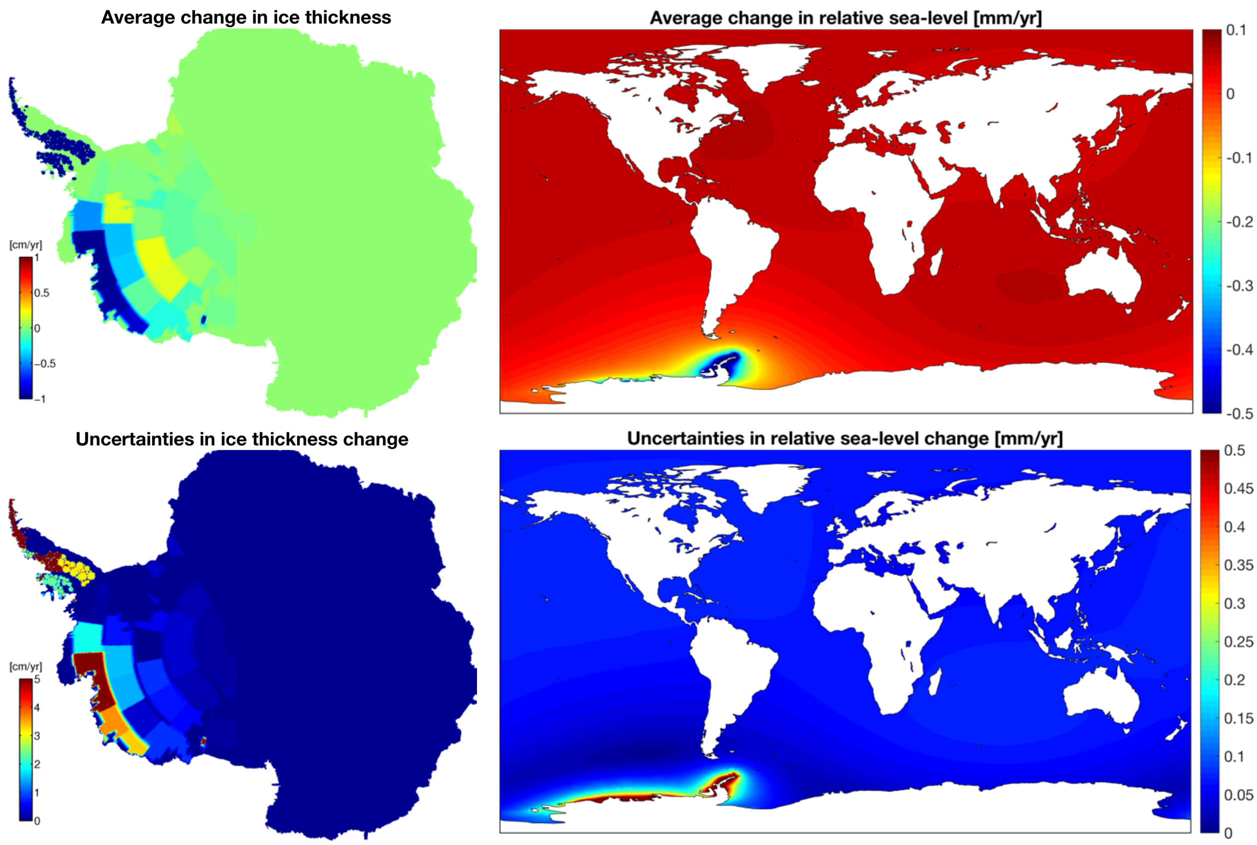

Figure S6 | AIS thinning and the associated sea-level rise. Only the Peninsula and the West AIS are assumed to have lost significant mass during the 20th century. Notice that mean loss signals considered in our analysis (top left) are much smaller than the uncertainties (lower left).

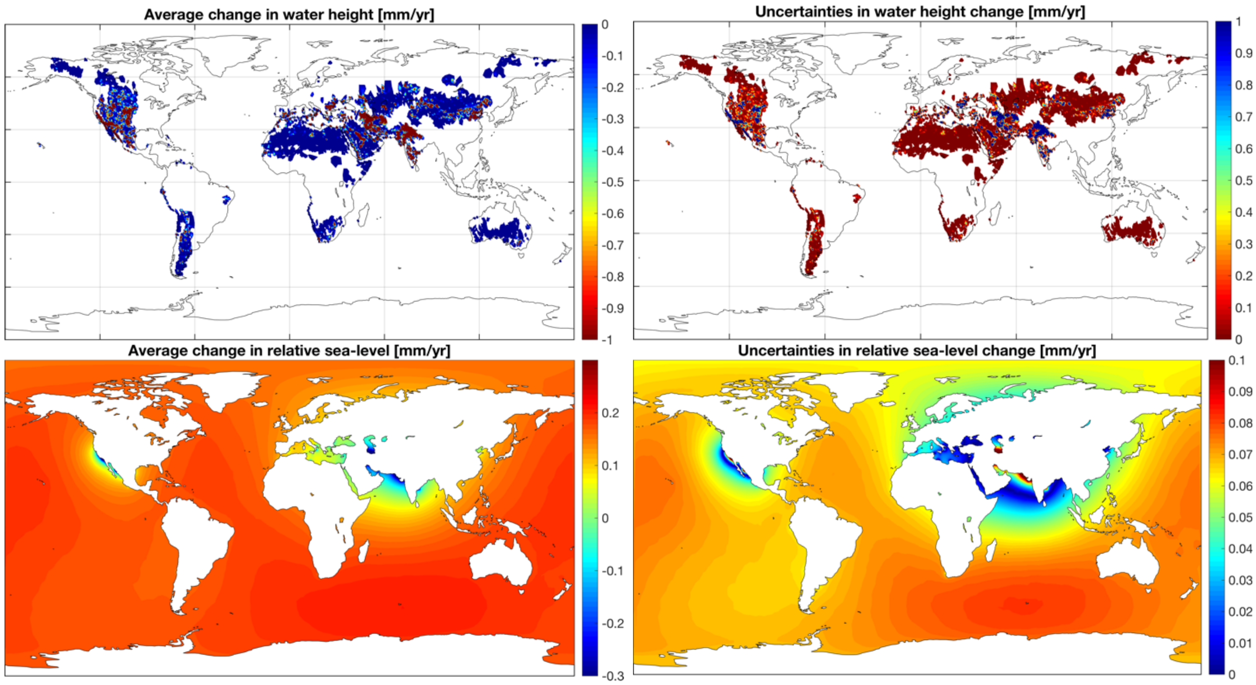

Figure S7 | 20th century rate of GWD and the associated rate of sea-level rise. Large depletions from the Indian subcontinent and western US (top left) are clearly reflected in the sea-level distribution map (bottom left). The same regions also have large uncertainties (right).

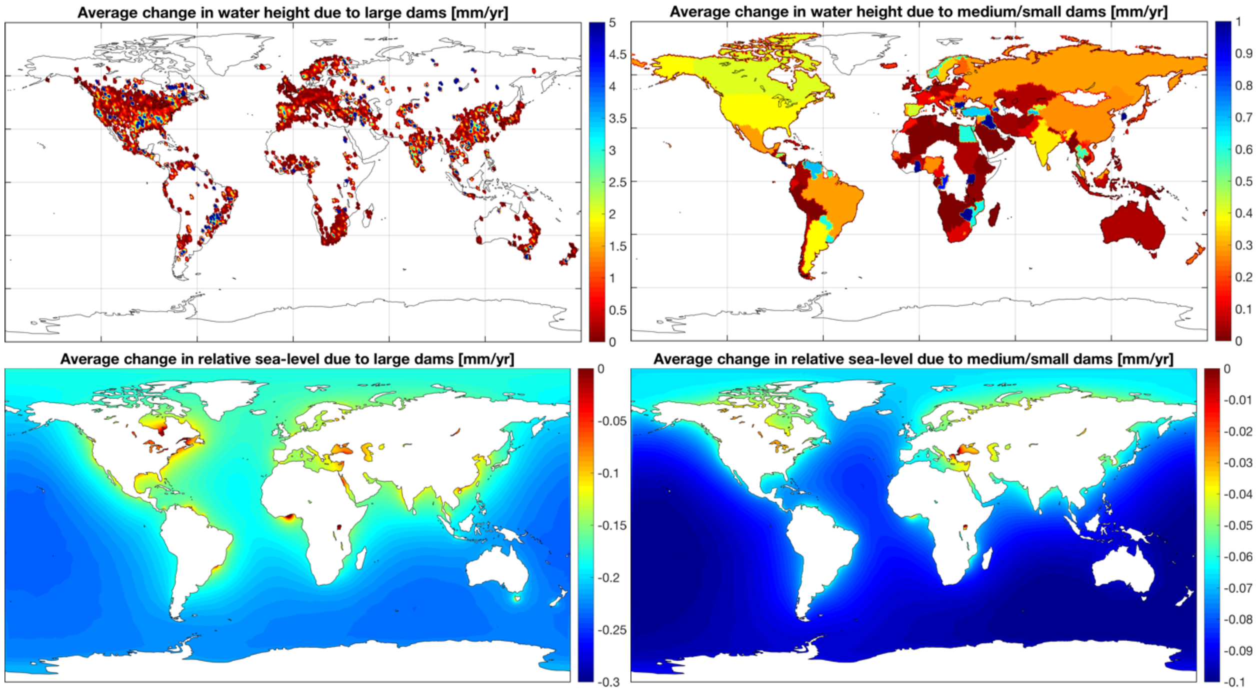

Figure S8 | 20th century RWI and the associated sea-level drop. Since the exact location of small dams are not known, we map the signal uniformly over the respective countries (top right). This approximation should affect our estimates of SPM, which is a function of degree-2 loading pattern (see equation S2), only minimally. These land hydrology maps (top) also account for seepage from the dams into the adjacent rock.

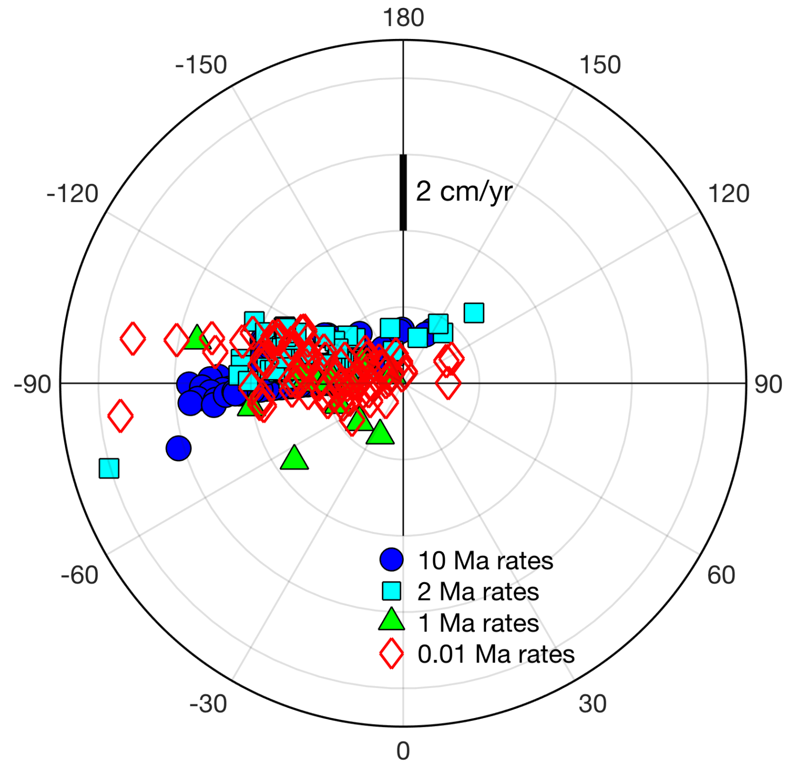

Figure S9 | Present rate of TPW due to mantle convection. We assemble 188 solutions for TPW rate, 94 each for the past 2 (squares) and 10 (circles) million years, from a suite of slab subduction driven forward models (Table S5). We perform a total of 95 new TPW predictions using a backward-advection approach (Table S6), of which we retrieve solutions for the last 1 (triangles) and 0.01 (diamonds) million years from 13 and 82 models, respectively. In general, all of these models yield westward motion of the spin axis, but with varying amplitudes. We only use 82 of these (diamonds) in Figure 4 as representative solutions, because results do not much depend on the time period of backward-advection. Note that TPW rates are computed in "mantle reference frame"; we project these onto the "mean lithospheric reference frame" in which both the observed and modeled SPM are evaluated. Although several estimates of relative rotation of reference frames are available [81], here we use one particular solution computed by Torsvik *et al.* [73]: the rotation of the lithospheric reference frame with respect to the mantle frame, over the last 5 million years, is about a Euler pole at 67.5° south latitude and 132.1° east longitude at a speed of 0.13°/Ma.